Research Square

Preprints are preliminary reports that have not undergone peer review.
They should not be considered conclusive, used to inform clinical practice,
or referenced by the media as validated information.

Patient-Specific Ipsc Model for Tbx5 Reveals Transcriptomic and Metabolic Disturbances Causing Holt–Oram Syndrome

Martina Dreßen

dressen@dhm.mhn.de

TUM University Hospital German Heart Center https://orcid.org/0000-0003-2200-6254

Bernd Northoff

University Hospital, Ludwig-Maximilians-University

Harald Lahm

TUM University Hospital German Heart Center

Irina Gottmann

TUM University Hospital German Heart Center

Sven Richter

TUM University Hospital German Heart Center

Dhammapal Bharne

TUM University Hospital German Heart Center

Felix Wirth

TUM University Hospital German Heart Center

Gertrud Goppel

TUM University Hospital German Heart Center

Sabine seeler

TUM University Hospital German Heart Center

Elda Dzilic

TUM University Hospital German Heart Center

Marina Reinsch

University Medical Center Hamburg-Eppendorf

Stefanie Doppler

TUM University Hospital German Heart Center

Arne Hansen

University Medical Center Hamburg-Eppendorf

Rüdiger Lange

TUM University Hospital German Heart Center

Jürgen Hörer

TUM University Hospital German Heart Center
Julie Cleuziou
TUM University Hospital German Heart Center
Daniel Teupser
University Hospital, Ludwig-Maximilians-University
Lesca Holdt
University Hospital, Ludwig-Maximilians-University
Markus Krane
TUM University Hospital German Heart Center

Article

Keywords:

Posted Date: October 7th, 2026

DOI: https://doi.org/10.21203/rs.3.rs-11267708/v1

License: This work is licensed under a Creative Commons Attribution 4.0 International License.
Read Full License

Additional Declarations: There is a conflict of interest Dr. Krane is a physician proctor and a member of the medical advisory board for JOMDD and has received speakers' honoraria from EDWARDS, AtriCure, and Medtronic. The other authors report no conflicts.

Abstract

Congenital heart defects are the most common congenital malformations, yet their mechanisms remain poorly understood. We generated the first patient-specific induced pluripotent stem cell model of Holt-Oram syndrome carrying the *TBX5* Pro85Thr mutation, along with a CRISPR-corrected isogenic control, to investigate developmental mechanisms underlying ventricular septal defects and tricuspid valve dysplasia. Using 2D cardiac differentiation and 3D human heart organoids, we identified impaired induction of key cardiac transcription factors (*TBX5*, *NKX2-5*, *GATA4*), consistent with disrupted first heart field lineage specification. Temporal and single-cell transcriptomic profiling further revealed altered developmental, contractile, and metabolic programs, across cardiac progenitors, cardiomyocytes, and endocardial-, endothelial-, and fibroblast-like cells, including myogenesis, sarcomere organization, oxidative phosphorylation, and lipid metabolism. At the functional level, mutant cardiomyocytes showed delayed structural maturation, reduced ATP production and glucose uptake, and increased cholesterol biosynthesis. Together, these transcriptional and metabolic alterations reveal developmental and maturation defects that provide a mechanistic framework for the patient's ventricular septal defects and dysplastic tricuspid valve with leaflet prolapse. Importantly, maturation defects and metabolic dysregulation were independently reproduced in cardiomyocytes derived from a second CRISPR-engineered isogenic *TBX5* Pro85Thr pair from a healthy male donor. Our findings identify disrupted cardiac metabolic maturation, characterized by impaired energy metabolism and cholesterol homeostasis, as a key downstream consequence of *TBX5* haploinsufficiency and provide broader mechanistic insight into *TBX5*-associated congenital heart defects.

Introduction

The heart is a highly energy-demanding organ composed of diverse cell types derived from distinct progenitors. Proper temporal and spatial regulation of progenitor induction, expansion, and lineage specification is essential for accurate cardiogenesis.[1]

Congenital heart defects (CHDs) are the most common birth defects, accounting for 28% of all congenital malformations, with a frequency of 9.1 per 1,000 live births.[2,3] CHD typically arises from defective cardiac morphogenesis and is generally considered multifactorial.[4] In addition to known causative genes[5], major chromosomal syndromes[6], *de novo* mutations[7], aneuploidy[8], and copy number variations[4,9,10] contribute to its aetiology.[11] However, the molecular pathways downstream of identified genetic causes remain poorly understood.[12]

Mutations in the transcription factor (TF) *TBX5*, cause Holt-Oram syndrome (HOS, OMIM #142900), a rare autosomal dominant heart-hand syndrome with an estimated prevalence between 0.7 and 1 per 100.000 births[13], first described by Holt and Oram in 1960[14]. HOS involves CHDs and/or arrhythmia and upper limb malformations[15,16], with high phenotypic variability. Atrial septal defects (ASDs) and ventricular septal defects (VSDs) are the most frequent cardiac anomalies, occurring alone or in

combination. *TBX5* belongs to the T-box family and is known for its importance in cardiomyogenesis, septation, and development of the conduction system [17], either individually or in combination with other TFs such as *NKX2-5* and *GATA4*.[18,19] Animal models have shown that Tbx5 is essential for tissue structuring[20] and its expression has been demonstrated during embryogenesis in the heart and upper limbs[21], consistent with HOS phenotypes. Its dosage-dependent role in heart morphogenesis has been mapped in mouse and zebrafish models.[22–29]

Diagnosing a patient with HOS should follow strict diagnostic criteria, requiring the presence of preaxial radial ray malformation in at least one upper limb along with a personal or family history of septal defects (ASD, VSD) and/or atrioventricular conduction disease.[30] A *TBX5* mutation is found in 70% of patients showing these criteria.[31]

From early cardiac progenitor cell (CPC) stage to lifelong function in cardiomyocytes (CMs) and non-myocyte cells, efficient mitochondrial activity and metabolic regulation are critical. During development, cardiac metabolism shifts: in the hypoxic fetal heart, ATP is primarily generated via glycolysis due to low fatty acid (FA) availability. After birth, increased oxygen and FA levels promote a switch to oxidative metabolism.[32,33] Similarly, induced pluripotent stem cell (iPSC)-derived CMs cultured in high-glucose, low-FA media rely on glycolysis, mimicking embryonic energy metabolism.

Mitochondria generate cellular ATP and rely on membranes enriched in cardiolipin and low in cholesterol, a balance crucial for structure and function.[34] Excessive levels of mitochondrial cholesterol disrupts membrane organization, impairs respirasome assembly, and compromises bioenergetics. [35] Given the heart´s high energy demand, tight control of mitochondrial cholesterol and overall energy metabolism in essential for normal cardiomyocyte and cardiac function.[36]

We established a patient-specific iPSC model from an individual diagnosed with HOS according to McDermott´s strict criteria[30], carrying a *de novo TBX5* mutation with severely reduced biological function[37]. This model captures early developmental stages to reveal dysregulation directly attributable to the mutation. Although iPSCs have been widely used to study genetic diseases[18,38–40], no patient-specific iPSC model for HOS has been reported previously. By comparing mutant and isogenic corrected iPSCs throughout cardiac differentiation, and validating key findings in an independent TBX5 mutant-control pair carrying the same mutation, we link the cardiac phenotype to the *TBX5* mutation, confirm its pathogenicity, and identify downstream molecular pathways contributing to CHD.

Results

Heterozygous de novo TBX5 mutation leads to Holt-Oram Syndrome, manifesting in a severe clinical phenotype

We identified a patient (1460) with a heterozygous *TBX5* mutation ($TBX5^{mut/WT}$) fulfilling the strict diagnostic criteria for HOS[30]. Preaxial radial malformations had been reported previously[37], and the mutation was confirmed as *de novo*[37], as neither parent carried the variant (Fig. 1a). A female sibling was unavailable for genetic testing due to geographical constraints; however, family history indicated a diagnosis of ASD (Fig. 1a) without limb malformation.

Electrocardiography confirmed sinus rhythm (Fig. 1b), while chest X-ray revealed cardiomegaly (Fig. 1c) with markedly increased cardio-thoracic ratio, as previously described[37]. Echocardiography identified VSDs (Fig. 1d) and a dysplastic tricuspid valve (TV) with prolapse of the anterior and short septal leaflets, causing regurgitation (Fig. 1e).

Sequencing confirmed the heterozygous point mutation rs1565941579: C > A in exon 4 of *TBX5* NM_181486.4, resulting in an amino acid substitution at position 85 from proline to threonine (NP_852259.1:p.Pro85Thr) (Fig. 1f, g). Our prior study predicted that this mutation induces a conformational change within the TBX binding domain.[37] The affected region is highly conserved across the TBX gene family and has remained preserved throughout evolution.[37] Functional assays demonstrated that the mutated TBX5 protein failed to activate the *NPPA* promotor - a known TBX5 target – while its subcellular localization remained unchanged, suggesting that impaired transcriptional activity is not caused by nuclear exclusion.[37]

Based on the detailed characterization of the *TBX5* mutation and the patient´s severe cardiac phenotype, we generated a patient-specific iPSC line 1460 ($TBX5^{mut/WT}$) from the patient´s adipose fibroblasts[41], obtained during planned VSD closure (Fig. 1h). To identify mechanisms that can be directly attributed to the *TBX5* mutation, we corrected the point mutation using CRISPR/Cas9 genome editing and generated the isogenic corrected line 1460c ($TBX5^{WT/WT}$)[42]. Sanger sequencing confirmed the presence of the heterozygous *TBX5* mutation in the iPSC line 1460 and its successful correction in the iPSC line 1460c (Fig. 1i). For independent validation in a second genetic background, the same Pro85Thr mutation was introduced into the healthy male donor-derived iPSC line L ($TBX5^{WT/WT}$)[43] using CRISPR/Cas9, generating the isogenic mutant line Lmut ($TBX5^{mut/WT}$)[44] (Fig. 1h).

To investigate developmental disorders during cardiogenesis, we performed longitudinal transcriptomic profiling of the 1460/1460c pair during 2D cardiac differentiation and 3D human heart organoid development. The Lmut/L pair was profiled at the iPSC and d14 cardiomyocyte stages to validate the findings in an independent genetic background. Downstream analyses included functional validation, integration with TBX5 ChIP-seq data, and gene-set enrichment analyses (GSEA) (Fig. 1j). Using the two isogenic pairs enabled us to isolate the effects of the patient´s *TBX5* mutation, directly link this genetic variant to the pathogenesis of the observed CHD, and validate associated molecular disturbances across independent genetic backgrounds.

In vitro analysis indicates dysregulation of core cardiac transcription factors in TBX5-mutated Cardiac Progenitor Cells and impaired Cardiomyocytes maturation

To define the *in vitro* phenotype, we performed 2D cardiac differentiation using Wnt modulation[40] (Fig. 2a). Bulk RNA-seq across key developmental stages (d06, cardiac intermediate stage; d08, CPC stage; d10, early CM stage; and d14, CM stage) confirmed progressive differentiation (Fig. 2b), as indicated by downregulation of pluripotency genes (*NANOG*, *POU5F1*, *SOX2*, and *UTF1*), and sequential induction of mesodermal (*EOMES*, *MESP1*, *MIXL1*, *TBXT*), progenitor (*ISL1*, *GATA4*), and cardiac markers (*TNNT2*, *MYH6*) in both the patient-specific iPSC line 1460 and the TBX5-corrected iPSC line 1460c, as expected[45] (Supplementary Data Set 1). Representative morphologies and extended differentiation data were analyzed (Fig. 2C, Supplementary Figure S1, Videos S1 to S6). RNA quality metrics, principal component analysis (PCA) and allele-specific expression confirmed dataset robustness (Supplementary Figure S2).

Stage-specific interaction analysis revealed genotype-dependent differences in transcriptional trajectories during cardiac differentiation (Fig. 2d). Genes with differential temporal regulation were already detectable at d06 and d08 and increased at later stages (Supplementary Figure S3, Dataset 2, 3).

To validate key transcriptional changes, fold induction normalized to iPSCs was assessed by qRT-PCR (Fig. 2e). *TBX5* induction was significantly lower in the mutant line 1460 ($TBX5^{mut/WT}$) compared to the corrected line 1460c ($TBX5^{WT/WT}$) at d08 and d14 (Fig. 2e). Notably, *TBX5* expression levels remained unchanged in 1460, while 1460c exhibited robust induction during cardiac differentiation.

Previous studies have shown that heterotypic TF interactions, particularly among *TBX5*, *NKX2-5*, and *GATA4*, are essential for coordinated cardiogenesis.[18,46] In our 2D *in vitro* model, *NKX2-5* expression levels were significantly altered at d08. Similar to *TBX5*, the mutated iPSC line 1460 showed no significant *NKX2-5* induction, whereas the corrected iPSC line 1460c exhibited significant upregulation during differentiation (Fig. 2e). Both lines showed progressive *GATA4* induction over time, but *GATA4* induction was significantly reduced in 1460 ($TBX5^{mut/WT}$) compared to 1460c ($TBX5^{WT/WT}$) at d06, d10, and d14 (Fig. 2e). Overall *ISL1* induction was higher in the mutated line, whereas only the corrected line 1460c showed significant temporal changes during differentiation (Fig. 2e).

NPPA, a known downstream target of TBX5, previously shown to be unresponsive to the mutated protein[37], displayed no significant induction in 1460 over time (Fig. 2e). *TNNT2*, a marker of CMs, was significantly induced in 1460c but not in 1460 during the first 14 days of differentiation (Fig. 2e), consistent with impaired cardiac maturation.

Immunostaining at day 30 confirmed sarcomeric (α-ACTININ, TNNT2) and junctional (CX40, CX43) protein expression in both lines (Fig. 2f).

To further characterize these early genotype-dependent transcriptional changes, we performed stage-resolved GSEA of cardiac-related biological processes (Fig. 2g). Early developmental programs, including heart growth, heart morphogenesis, and cardiac muscle cell proliferation, were enriched at d06/d08, whereas later stages were associated with cardiac contraction and ventricular cardiac muscle cell

differentiation. GSEA also revealed negative enrichment of actomyosin structure organization at d08 in the mutant condition (Fig. 2h), indicating early dysregulation of structural cardiac programs. Consistent with this finding, immunostaining at day 30 showed a more elongated sarcomeric organization in corrected cells (Fig. 2i). Correspondingly, quantitative analysis revealed significantly shorter sarcomeres in 1460-derived CM (Fig. 2j), consistent with reduced maturation.

Overall, TBX5 haploinsufficiency severely impaired induction of key cardiac TFs, particularly those associated with first FHF lineages. These dysregulations were accompanied by early alterations in cardiac developmental and structural programs and may underlie the reduced maturation observed in patient-derived CMs, further emphasizing the pathogenic role of the *TBX5* mutation in disrupting early cardiac developmental programs and subsequent cardiomyocyte maturation.

Single-cell RNA sequencing of beating TBX5-mutated Cardiac Progenitor Cells uncovers disrupted energy metabolism and cholesterol homeostasis

Given the early disturbance of cardiac TF induction, we focused on d08 cardiac cells, marking the transition from CPCs to early beating CMs. Isogenic lines (1460/1460c) were differentiated in parallel, and single-cell RNA sequencing (scRNA-seq) was performed on beating CPCs at d08, yielding high-quality transcriptomes (Fig. 3a, Supplementary Figure S4a-c). Unsupervised clustering identified 13 distinct cellular subpopulations (Fig. 3b), with broad *TNNT2* expression confirming efficient cardiac differentiation (Fig. 3c). Top marker genes for each cluster are displayed in the heatmap (Fig. 3d, Supplementary Data Set 4). Canonical marker analysis, enabled annotation of major CPC states (clusters 0–7) and minor non-cardiac populations (cluster 8–12) (Fig. 3e, f, Supplementary Data Set 5).

Genotype-based distribution (Fig. 3g) showed consistent clustering across replicates (n = 2 per iPSC line, Fig. 3h), with CPCs dominated both datasets (Fig. 3h). Notably, early CPC clusters (0, 7) were significantly enriched in 1460, whereas more advanced CPCs (cluster 1–5) were reduced indicating delayed lineage progression (Fig. 3h). Thereby, cluster 7 is of particular interest as it comprises 20% of all 1460 cells (Fig. 3h, i). Taken together, the overrepresentation of 1460 cells in cluster 7 (CPC) and their reduced presence in clusters 1 to 5, representing more advanced cardiac stages, suggest a delay in cardiogenesis in the 1460 cell line, likely caused by disrupted cardiac lineage commitment due to impaired induction of cardiac TFs.

To further investigate the impact of the heterozygous loss-of-function mutation on cardiogenesis, we focused on clusters 0 to 7, representing the majority of cardiac cell populations (Supplementary Figure S4d), defined in the following as cardiac progenitor cells (CPCs) in general, and excluded clusters 8 to 12 from downstream analysis. Differential expression analysis of CPC clusters (0–7) revealed broad metabolic dysregulation in 1460 cells. Key pathways - including glycolysis, TCA cycle, mitochondrial electron transport, and oxidative phosphorylation were consistently downregulated (Fig. 3j, Supplementary Figure S5a to d, Data Set 6). In detail, reduced expression of the glucose-transporter GLUT1 (*SLC2A1*), multiple glycolytic enzymes (*GPI*, *GAPDH*, *PGK1*, *ENO1*, *PKM*), the Lactate dehydrogenase A (*LDHA*), crucial for NAD^+ regeneration via pyruvate to lactate conversion, the TCA cycle

component succinyl-CoA synthetase (*SUCLG1*), responsible for the only substrate-level phosphorylation step in the TCA cyle, and mitochondrial complex I–V genes (complex I/NADH-dehydrogenase: *MT-ND1*, *MT-ND2*, *MT-ND4*, *MT-ND5*, complex III/cytochrom-c-reductase: *MT-CYB*, complex IV/cytochrom-c-oxidase: *MT-CO1*, *MT-CO2*, *MT-CO3*, and ATP synthase: *ATP5F1B*, *MT-ATP6*, oxidative phosphorylation) was decreased expressed (Fig. 3j, Supplementary Figure S5a to d, Data Set 6). Conversely, cholesterol biosynthesis and homeostasis genes were strongly upregulated in 1460 CPCs, including *HMGCS1*, *HMGCR*, *IDI1*, *FDFT1*, *SQLE*, *MSMO1*, *CYP51A1*, *NSDHL*, and *SC5D(L)* (Fig. 3j, Supplementary Figure S5e, Data Set 6). Notably, expression of *INSIG1*, which encodes an endoplasmic reticulum membrane protein regulating cholesterol metabolism and glucose homeostasis by mediating ubiquitin-dependent degradation of HMGCR, the rate-limiting enzyme in cholesterol synthesis, was significantly elevated in the mutated 1460 CPCs (Supplementary Figure S5e). In summary, scRNA-seq analysis revealed an early-stage bias in HOS patient-specific CPCs, marked by impaired cardiac lineage progression and profound metabolic and cholesterol pathway dysregulation.

Multicellular 3D-Model of TBX5-mutated Human Heart Organoids reveals disruptions in energy metabolism, cholesterol homeostasis, and cytoskeletal architecture

Self-organizing human heart organoids (hHOs) were generated by sequential Wnt-modulation, forming beating 3D aggregates that recapitulatecardiogenesis *in vitro*[47] (Fig. 4a, b, Supplementary Videos S7 to S10).

Transcriptomic profiling (bulk RNA-seq) of the hHOs at d08, d10, and d15 confirmed robust differentiation in both isogenic lines, with expression of FHF, SHF, early/late cardiac, as well as as epicardial, endothelial, fibroblast and extracellular matrix (ECM) genes validating hHOs[47] as a suitable model for studying *TBX5*-related cardiogenesis (Supplementary Figure S6a to c, Data Set 7). Time resolved analysis revealed widespread transcriptional changes in mutant hHOs: 1,063 (d08), 866 (d10), and 773 (d15) downregulated genes, with 150 shared across all stages (Fig. 4c, Supplementary Data Set 8). In parallel, 294 (d08), 680 (d10), and 334 (d15) genes were upregulated, including 51 consistently affected across time points (Fig. 4c, Supplementary Data Set 8).

TBX5 expression was increased in corrected 1460c hHO at d10 and d15, with similar increases in *GATA4* and *NKX2-5*, known for their heterotypic interaction with TBX5 (Fig. 4d, Supplementary Figure S6d). FHF marker *HAND1* was significantly reduced in mutated 1460 hHOs at day d08 and d10, while *MEF2C* and *ISL1* (early CPC markers/SHF markers) remained unchanged (Fig. 4d, Supplementary Figure S6d). Atrial/early CM markers (*MYH6*, *MYL7*) showed no differences, but ventricular CM markers (*MYH7*, *MYL2*) were reduced at day 15 (Fig. 4d, Supplementary Figure S6d). Immunostaining confirmed these trends - α-ACTININ (Supplementary Figure S7a) and MLC2A encoded by *MLY7* (Supplementary Figure S7b) were unchanged, whereas MLC2V, coded by *MYL2* was reduced in mutated 1460 hHO (Supplementary Figure S7c).

Endocardial markers *TEK* and *ENG* were downregulated in the mutated hHOs, with TEK significantly reduced at all timepoints (Fig. 4d, Supplementary Figure S6d), indicating impaired endocardial development, which is critical for endocardial cushion and septum formation. Expression of the cardiac fibroblast/epicardial marker *WT1* was significantly reduced in the mutated hHOs, alongside decreased *DDR2* levels (Fig. 4d, Supplementary Figure S6d). Endothelial markers *vWF* was less expressed, accompanied by concomitant decrease in *FLT1* and *VEGFC* (Fig. 4d, Supplementary Figure S6d). Additionally, ECM genes *COL1A1* and *DCN* showed strongly downregulation, with almost no expression in the mutated hHOs (Supplementary Figure S6d). Together, these changes point to disrupted endocardial, endothelial, fibroblast, and ECM maturation.

Comparison with single-cell transcriptomic data of human fetal hearts (4.5 to 25 weeks gestation)[48], revealed that downregulated genes in mutated 1460 hHOs at d10 and d15 were enriched in CMs, particularly trabecular atrial CMs (CM A trab) and atrial CMs at 5 weeks (CM A 5-weeks), and at d15 also in right atrial CMs (CM RA) (Fig. 4e, Supplementary Data Set 9). Genes consistently reduced across all time points were mainly associated with left ventricular (CM LV), compact ventricular (CM V comp), and general ventricular CMs at 5 weeks of gestation (CM V 5-weeks) (Fig. 4e, Supplementary Data Set 9), indicating impaired FHF-derived ventricular development, while SHF and atrial CMs were less affected. Based on this data[48], downregulated genes in 1460 hHOs were also enriched in fibroblasts-like cells (FB like), endothelial cells (ECs) and valvular cells (Fig. 4e, Supplementary Data Set 9), indicating dysregulation beyond CMs and suggesting broader dysregulation across multiple cardiac lineages.

GSEA (Fig. 4f) revealed enrichment of pathways related to cell fate, patterning, and maintenance in mutated hHOs, whereas metabolic processes were consistently downregulated across all time points (Fig. 4f, Supplementary Data Set 10). At d15, normalized enrichment scores (NES) further indicated reduced expression of genes related to sarcomere organization, myogenesis, and oxidative phosphorylation (Fig. 4g, Supplementary Data Set 11), supporting defects in maturation and metabolism in *TBX5* mutated hHOs.

Validation of metabolic disturbances and TBX5 binding to metabolic regulators in HOS-derived Cardiac Progenitor Cells and early Cardiomyocytes

ATP production was significantly reduced in *TBX5* mutant line 1460 at d08 of the 2D differentiation and remained lower than in the corrected line (1460c) throughout differentiation (Fig. 5a). Only the corrected line showed significant ATP modulation indicating impaired metabolic adaptability to developmental demands in the mutant (Fig. 5a). Glucose uptake was higher in the corrected line (1460c) at d10, and although cholesterol increased in both lines, the mutant consistently showed higher levels (Fig. 5a), supporting transcriptomic findings in CPCs at d08.

Published TBX5 ChIP-seq data in iPSC-derived cardiomyocytes[18] revealed broad promoter-associated TBX5 occupancy and enrichment of cardiac developmental and structural programs among TBX5 target genes (Fig. 5b, c, Supplementary Data Set 12, 13).

Integration with the 2D differentiation model showed perturbation of selected cardiac developmental and metabolic GO-BP terms across d06 to d14 and identified temporally structured sets of TBX5-overlapping leading-edge genes in both categories (Fig. 5d to f). Both cardiac developmental and metabolic leading-edge genes were enriched among TBX5 promoter targets across differentiation stages (Fig. 5e, f, Supplementary Data Set 14).

To validate these findings in an independent genetic background, the *TBX5* Pro85Thr mutant line Lmut and its corresponding isogenic control line L were analyzed at d14 in parallel with 1460 and 1460c (Fig. 5G). Semantically related GO-BP terms showed concordant enrichment across both genetic backgrounds, including ventricular cardiac muscle cell differentiation, cardiac muscle cell contraction, and energy derivation by oxidation of organic compounds (Fig. 5h, Supplementary Data Set 15).

Analysis of TF–associated gene sets (MSigDB C3 TFT) also revealed concordant regulatory disturbances across both genetic backgrounds (Fig. 5i). Cardiac developmental and oxidative metabolic programs showed negative enrichment at d14 in both mutant lines, whereas E2F-associated programs showed concordant positive enrichment (Fig. 5i, Supplementary Data Set 16).Overall, metabolic assays showed reduced ATP production, altered glucose uptake, and elevated cholesterol in *TBX5* mutant cells, aligning with transcriptomic and ChIP-seq evidence of disrupted metabolic and structural maturation with concordant developmental, metabolic, and regulatory disturbances in an independent genetic background.

Discussion

In the patient analyzed here, a *de novo* heterozygous point mutation resulting in an amino acid change (Pro85Thr) was identified and previously characterized in detail.[37] The observed cardiac defects - multiple VSDs and a dysplastic TV – align with the known spatial and temporal expression pattern of TBX5[49] and are consistent with phenotypes reported in related studies. Although downstream targets of TBX5[19,23,24,50], and ChIP-seq data for WT-TBX5[18] have been explored, comprehensive insights into the mechanistic impact of TBX5 remain incomplete. In particular, how *TBX5* mutations affect cardiac development at the cellular level, especially within anatomically affected regions, remains elusive. This knowledge would help correlate genotype with phenotype more precisely and uncover the underlying pathophysiological mechanisms.

To investigate the impact of this particular *TBX5* point mutation (Pro85Thr)[37] associated with the severe cardiac phenotype of the HOS patient, we generated a patient-specific iPSC line 1460 ($TBX5^{mut/WT}$)[41] and corrected the mutation using CRISPR/Cas9 to create an isogenic control 1460c ($TBX5^{WT/WT}$)[42]. Additionally, we generated a control line L ($TBX5^{WT/WT}$)[43] and the corresponding isogenic mutant line Lmut ($TBX5^{mut/WT}$)[44] for independent validation across a second genetic background. These isogenic iPSC pairs, differing only by the *TBX5* mutation, enable direct attribution of observed developmental disturbances to the mutation itself, while minimizing confounding effects of genetic background.

Notably, only one human iPSC model for HOS exists, but it lacks patient specificity and carries a homozygous TBX5 deletion[51] – genotypes not observed in patients and embryonically lethal in mice[19]. Thus, our patient-specific model provides a unique and physiologically relevant system to study HOS-related TBX5 dysfunction. Combined with isogenic CRISPR-correction and multi-level analyses, this model enables detailed investigation of TBX5-dependent mechanisms during human cardiac development.

Using complementary 2D[52] and 3D[47] *in vitro* models, we investigated the developmental consequences of the patient-specific *TBX5* Pro85Thr mutation using isogenic iPSC lines (1460: $TBX5^{mut/WT}$, 1460c: $TBX5^{WT/WT}$). Both systems recapitulated early cardiogenesis and revealed transcriptional disturbances consistent with disrupted TBX5-dependent regulatory networks.

Given the essential cooperative interactions among TBX5, NKX2-5, and GATA4[18,19,46,50,53,54], the previously demonstrated functional TBX5 haploinsufficiency[37] in the 1460 line resulted in impaired induction of these TFs and downstream cardiac markers, whereas the isogenic control displayed normal temporal activation. This confirms that TBX5 loss perturbs broader TF networks[18,19,55–59], producing temporally and spatially altered expression patterns. The 3D hHO model corroborated these findings, showing selective downregulation of FHF markers in the mutated line 1460, while later CPC markers associated with SHF specification remained unaffected. Notably, ventricular CM markers (MYL2/MLC2V, MYH7) were reduced at both transcript and protein levels in 1460 and were accompanied by shorter sarcomeres, indicating impaired ventricular maturation. Together, these findings are consistent with early TF dysregulation leading to impaired FHF specification and delayed structural maturation.

Our HOS patient-specific iPSC model carrying the *TBX5* Pro85Thr mutation, together with the pronounced CM maturation defects observed, prompted a focused analysis of day 8 CPCs (1460/1460c), the stage at which contraction initiates and progenitors transition towards early CMs. scRNA-seq at (d08) revealed an overrepresentation of early progenitor states and a lack of more advanced cardiac fates in the mutated line 1460, supporting a delay in lineage progression and cardiomyocyte maturation.[18,40]

The patient presented with multiple trabecular (“swiss-cheese”) VSDs and a dysplastic TV. Trabecular VSDs arise within the muscular interventricular septum (IVS), which is primarily composed of CMs, fibroblast-like cells and endothelial cells[48,60]. The hHO model enabled assessment of these lineages beyond CPCs and CMs. The *TBX5*-mutated line (1460) showed reduced expression of endocardial markers, suggesting impaired endocardial cushion formation - a known driver of septal defects. Dysregulation in fibroblast-like and endothelial markers further supports their contribution to the observed phenotype. Together, these findings indicate that the *TBX5* mutation perturbs multiple IVS relevant cell populations, providing a mechanistic link to the patient’s multiple trabecular VSDs.

Heart valves develop from endocardial cushion tissue, and defective cushion formation is a well-established cause of atrioventricular valve malformations.[61–64] Major valve cell types include valvular

fibroblasts (valvular interstitial cells, VICs), valvular endothelial cells (VECs) and immune cells.[65–67] In our 3D hHO model, the *TBX5*-mutated line 1460 showed dysregulation of key valvular markers, particularly fibroblast- and endothelial-associated genes such as *COL1A1* and *DCN*[48]. These alterations in VIC- and VEC-associated lineages provide a mechanistic link to the dysplastic TV and regurgitation observed in the HOS patient.

Taken together, the downregulated genes in the *TBX5*-mutated 1460-hHO map to cell populations that contribute to the IVS and TV, consistent with Cui et al.[48]. Thus, our model links *TBX5*-dependent lineage disturbances in IVS- and TV-forming cell populations to the patient's structural cardiac phenotype.

To define how TBX5 haploinsufficiency contributes to cardiac malformations, we examined metabolic alterations in CPCs/early CMs (1460/1460c) that may underlie IVS and TV defects. During embryonic cardiogenesis, ATP production depends largely on glycolysis due to the hypoxic environment and low FA availability[32,33], a profile recapitulated during iPSC-CM differentiation. At day 8, scRNA-seq revealed reduced expression of the glucose transporter *SLC2A1* and broad suppression of glycolysis, the TCA cycle, and oxidative phosphorylation, including impaired mitochondrial electron transport from NADH to ubiquinone. In contrast, cholesterol biosynthesis and homeostasis pathways were upregulated. Metabolic assays and 3D hHO model confirmed dysregulation of energy metabolism and cholesterol pathways. Importantly, leading-edge analysis identified genes driving cardiac developmental and metabolic pathway enrichment that overlapped with published TBX5 ChIP-seq targets, supporting a link between TBX5-dependent transcriptional control, cardiac development, and metabolic regulation. Impaired cardiac developmental and oxidative metabolic programs were reproduced at day 14 in the independent Lmut/L background, whereas E2F-associated programs showed concordant positive enrichment. Together, these findings support shared disruption of developmental and metabolic maturation across genetic backgrounds. As E2F1 has been shown to promote glycolysis and to limit mitochondrial glucose oxidation[68], two features of the Warburg effect, this opposing pattern may reflect disrupted coordination between cell cycle regulation and oxidative maturation during cardiomyocyte differentiation, consistent with delayed maturation in the mutant lines.

These findings align with Steimle et al., who interrogated the cardiac transcriptome of left ventricular tissue from a 10-year-old female HOS patient presenting a *TBX5* mutation (Pro85Arg) at the same amino acid position as in the patient analyzed here (Pro85Thr), along with additional mutations in *DNHD1* and *ZNF469*.[69] Using TBX5 ChIP-seq of iPSC-derived CMs, the study revealed that approximately 20% of direct TBX5 target genes are linked to metabolic pathways - including glucose and glycogen metabolism, the TCA cycle, and amino acid synthesis – highlighting the poorly understood role of TBX5 in metabolic regulation.[69] Moreover, ChIP-seq data by Ang et al.[18] identified TBX5-regulated genes involved in cardiac differentiation, ATP-dependent activity, glucose transport, and mitochondrial function. Together with the enrichment of published TBX5 targets among our leading-edge genes and the shared metabolic signatures observed across two genetic backgrounds, these ChIP-seq data support a role for TBX5 in cardiac metabolic regulation. These data indicate that *TBX5* mutations disrupt metabolic programming

required for proper development of IVS and TV cell populations, linking transcriptional dysregulation to the observed CHDs.

Mitochondrial membrane integrity is crucial for cardiac function, relying on a lipid composition enriched in cardiolipin and naturally low in cholesterol.[34] Elevated cholesterol perturbs membrane organization, disrupts respirasome assembly, and impairs bioenergetics[35], a vulnerability of particular relevance given the heart´s exceptionally high energy demand.[36] In our *TBX5*-mutated iPSC model, scRNA-seq revealed robust upregulation of genes involved in cholesterol biosynthesis and homeostasis, accompanied by increased cholesterol levels. Thus, altered cholesterol homeostasis may further impair the energetic deficit by compromising mitochondrial membrane organization and respiratory function. Notably, metabolic dysregulation, especially mitochondrial impairment, is a well-established contributor to CHDs and other cardiac pathologies[70–76], but has not previously been demonstrated in *TBX5*-associated HOS.

Previous iPSC models, including those harboring *GATA4* and *PKP2* mutations, have demonstrated impaired glycolysis, altered mitochondrial function, and shifts in metabolic enzyme expression, linking these perturbations to reduced contractility and disease phenotypes. [18,77] In the cardiac context, Farhat and colleagues showed that genetic and metabolic cues actively shape lineage trajectories, identifying key glycolytic enzymes as drivers of endothelial-to-mesenchymal transition within the endocardium.[78] Together, these studies underscore metabolism as a central determinant of cardiac cell behavior and disease pathophysiology, reinforcing its relevance to the metabolic disturbances observed in *TBX5*-associated cardiac malformations.

Despite advances in genetic diagnostics, the etiology of many CHDs remains unresolved, even when a pathogenic variant is identified. This is particularly evident for cardiac transcription factors such as *TBX5*, where genotype–phenotype relationships are difficult to establish due to complex TF interactions, dose-dependent effects, and the precise spatial and temporal regulation required for cardiac development.[1,52–54,56] Additionally, each patient´s unique genetic background contributes to phenotypic variability: the same TF mutation can result in distinct CHDs, while different TF mutations may converge on similar malformations, underscoring the multifactorial nature of CHD pathogenesis.[79] Despite this genetic variability, the concordant developmental, contractile, metabolic, and regulatory signatures observed in the 1460/1460c and independent Lmut/L pairs indicate that key molecular consequences of the Pro85Thr mutation are retained across distinct genetic backgrounds, while line-specific differences may contribute to phenotypic variability. Metabolic state may represent an additional modifier, as differences in energy metabolism and cholesterol homeostasis could influence lineage fate and cardiac morphogenesis depending on developmental timing, spatial context, and genetic background.

A limitation of this study is that no ChIP-seq experiments were performed for the specific TBX5 mutation analyzed here. Instead, we relied on previously published ChIP-seq datasets generated for wild-type TBX5. As a result, mutation-dependent changes in DNA binding could not be assessed directly, limiting mechanistic interpretation of the enrichment of published TBX5 targets among developmental and metabolic leading-edge genes. Although key developmental, metabolic, and regulatory findings were

reproduced in an independent *TBX5* mutant-control pair, future studies should include additional *TBX5* mutations to determine which observed effects reflect shared pathogenic principles and which ones are mutation-specific mechanisms.

Our patient-specific iPSC model carrying a *TBX5* mutation revealed early metabolic and mitochondrial dysregulation in CPCs and nascent CMs, suggesting impaired developmental trajectories. These disturbances likely affect multiple cell populations contributing to the IVS and TV, including cardiomyocytes, fibroblast-like cells, and endothelial lineages. Together, our findings indicate that TBX5 haploinsufficiency disrupts transcriptional and metabolic programs during early cardiogenesis, thereby impairing lineage progression and cardiac metabolic maturation. This provides a mechanistic framework linking *TBX5* haploinsufficiency to the structural cardiac defects underlying congenital heart disease in HOS.

Materials and Methods

Clinical in vivo cardiac assessment

Electrocardiogram

Electrocardiogram was performed using the Schiller Cardiovit AT-102 plus.

Echocardiography

Transesophageal echocardiogram (TEE) was performed using a GE Vivid 95 ultrasound system equipped with a GE 9T transesophageal probe.

Patient-Specific iPSC-Derived Cellular Models

Cell line generation

A patient-specific iPSC line (1460) was established from adipose fibroblasts (AFs) of a 15-month-old male patient diagnosed with HOS using Sendai virus-mediated reprogramming according to a previously published protocol.[40] The corresponding isogenic iPSC line (1460c) with the corrected heterozygous mutation in the *TBX5* gene was generated using CRISPR/Cas9 genome editing. Both lines (DHMi004-A, DHMi004-A-1) are registered in the hPSCreg® database, fully characterized, and published.[41,42]

A healthy control iPSC line (L) was generated from AFs obtained from a 29-year-old male donor. The corresponding isogenic iPSC line carrying the patient-specific heterozygous *TBX5* mutation (Lmut) associated with HOS was produced using CRISPR/Cas9 genome editing. Both lines (DHMi005-A, DHMi005-A-1) are registered in the hPSCreg® database, fully characterized, and published.[43,44]

Informed consent

was signed by the legal guardians and the healthy proband. Procedure was approved by the local ethics committee of the medical faculty of the Technical University of Munich (Project number 5943/13; 285/17S).

iPSC- and iPSC-derived 2D- and 3D-cell culture

iPSCs were maintained and differentiated into iPSC-derived cardiac progenitor cells (iPSC-CPCs) and subsequently cardiomyocytes (iPSC-CM) as previously described.[41,42]

Differentiation of iPSCs into human heart organoids (hHOs) was performed as described by Lewis-Israeli et al.[47] with modifications. The original 96-well protocol was adapted to generate organoids in 6-well plates placed on an orbital shaker. Plates were coated with 1% Pluronic-F127 (Sigma-Aldrich, #P2443) in PBS for 24h, and washed three times with PBS to create an ultra–low-attachment surface. To initiate organoid formation, single-cell suspension of 300,000 cells per well was seeded in 3 mL hiPSC maintenance medium containing 10 µM Y-27632 (Tocris, #1254). Plates were placed on an orbital shaker at 70 rpm for duration of the experiment and incubated at 37°C, 5% O_2, and 5% CO_2 for 24h. The following day, Y-27632 was removed. All subsequent medium changes were performed as two-third exchanges by aspirating 2 mL spent medium and adding 2 mL fresh medium to minimize organoid disturbance. On day 0, mesoderm induction was initiated by adding the canonical Wnt activator CHIR99021 (4 µM; Sigma-Aldrich, #SML1046), BMP-4 (1.25 ng/mL; R&D Systems, #314-BP), and Activin A (1 ng/mL; R&D Systems, #338-AC). Reported concentrations reflect final working concentrations after two-third medium change. From day 0, the base medium was replaced with RPMI 1640 (Gibco, #61870-010) supplemented with 2% B27 without insulin (Thermo Fisher Scientific, #A1895601). On day 1, two-third medium change with base medium was performed to dilute the Wnt agonists. On day 2, Wnt inhibitor Wnt-C59 (2 µM; Selleck Chemicals, #S7037) was added, and cultures were transferred to normoxic conditions (37°C, 5% CO_2). On day 4, Wnt-C59 was removed with a basal medium change. On day 6, insulin (2 µg/mL, Sigma-Aldrich, #I9278) was added to the basal medium and included in all subsequent changes. On day 7, organoids were exposed to 2 µM CHIR99021 (1h), followed by replacement with basal medium. Organoids were then fed every other day (days 9, 11, 13) with basal medium. On day 15, organoids were washed with PBS, fixed in Histofix (Roth, #P087) for 1h, and washed twice with PBS.

Genomic and transcriptomic profiling

Verification of the *TBX5* mutation and the correction of the *TBX5* mutation

DNA was isolated using the DNeasy Blood and Tissue Kit (Qiagen, #69506) according to the manufacturer´s recommendations. Isolated DNA at 200 ng/µL was amplified with the Fast Start High Fidelity PCR-System (Merck, #4738292001) using 1x PCR reaction buffer containing 1.8 mM $MgCl_2$, 0.4 µM primers: hu*TBX5*_mut_F8612/hu*TBX5*_mut_R919 (forward 5´ GTTACCTCCTCCCTTCG CTTT 3´, reverse 5´ CAACCTGTGGGTGCAGCAATAG 3´), 0.2 µM dNTPs each, 5% DMSO, and 0.5 U Start High

Fidelity Enzyme Blend in a final volume of 20 µL. PCR products were purified and verified by Sanger sequencing (Eurofins Genomics GmbH, Ebersberg, Germany).

RNA isolation, reverse transcription PCR, and quantitative real-time PCR

Total RNA was purified using the peqGOLD total RNA kit (VWR International; #13-6834-02) and reverse transcribed into cDNA with M-MLV reverse transcriptase (Invitrogen™, Thermo Fisher Scientific, #28025013) according to manufacturer´s specification. Expression of *TBX5* (forward 5' TGATCATAACCAAGGCTGGA 3', reverse 5' GATTAAGGCCCGTCACCTTC 3'), *NKX2-5* (forward 5' TTCTATCCACGTGCCTACAGC 3', reverse 5' CTGTCTTCTCCAGCTCCACC 3'), *GATA4* (forward 5' GGAAGC CCAAGAACCTGAAT 3', reverse 5' GCTGGAGTTGCTGGAAGC 3'), *ISL1* (forward 5' GCAGCCCAATGACAAAACTAA 3', reverse 5' CCGTCGTGTCTCTCTGGACT 3'), *NPPA* (forward 5' GAGCGGACTGGGCTGTAAC 3', reverse 5' GGAGCCTCTTGCAGTCTGTC 3'), and *TNNT2 (*5' ATGATGCATTTTGGGGGTTA 3', reverse 5' TCCTCCTCTCAGCCAGAATC 3') was evaluated on a Quant Studio 3 (Thermo Fisher Scientific) using 0.3 µM of forward and reverse primer, 1 µL cDNA, and the Power SYBR® Green PCR Master Mix (Thermo Fisher Scientific, #4368708) according to the manufacturer´s instruction. Gene expression was normalized to β-*ACTIN* (forward 5' CCAACCGCGAGAAGATGA 3', reverse 5' CCAGAGGCGTACAGGGATAG 3'). Data are presented as fold induction over gene expression in iPSCs.

Bulk RNA-seq of 2D-cell culture

Transcriptomic profiling of 2D cultures was performed using iPSCs, iPSC-derived CPCs (d06, d08), and iPSC-derived CMs (d10, d14). RNA was isolated using the peqGOLD Total RNA kit (VWR International, #13-6834-02). For each iPSC line, two independent differentiation experiments were conducted. RNA samples were pooled per differentiation, resulting in biologically independent duplicate samples for each line and time point.

For RNA-seq, 50–150 ng total RNA was depleted of ribosomal RNA using the NEBNext rRNA Depletion Kit v2 (NEB, E7400) and reverse transcribed using SuperScript IV reverse transcriptase (ThermoFisher, 18090010). Double-stranded cDNA was generated using the TargetAmp kit (Epicentre, TAN091096) and tagmented using the Illumina Tagment DNA TDE1 Enzyme and Buffer Kits (Illumina, 15027916). Libraries were amplified using the KAPA HiFi HotStart Library Amplification Kit (Roche, KK2612) with unique dual indexes (IDT for Illumina Nextera). Libraries were purified, quantified by Qubit, and quality-controlled using a Agilent 2100 Bioanalyzer (Agilent Technologies) using the Agilent RNA 6000 Nano Kit (Agilent Technologies, 5067 – 1511). Sequencing was performed as 2 × 150 bp paired-end reads on a NovaSeq 6000 system (Illumina). Demultiplexing was performed using bcl2fastq (Illumina, v2.20).

Bulk RNA-seq of 3D-cell culture

For down-stream bulk RNA-seq, organoids were harvested (d08, d10, d15) and stored in liquid nitrogen. Organoids were transferred into 900 µL QIAzol lysis reagent and homogenized on dry ice using an Ultra

turrax MICCRA D-8 (ART Moderne Labortechnik) at 29,000 rpm. Total RNA was isolated using the QIAGEN RNeasy Plus Kit (Qiagen, #73404). RNA quality was assessed with the Agilent 2100 Bioanalyzer (Agilent Technologies). Subsequent library preparation, sequencing, and data processing were performed as described for RNA-seq of 2D cultures.

single-cell RNA sequencing (scRNA-seq)

Cells were dissociated (d08) using 10x TrypLE Select (Thermo Fisher Scientific, #A1217702), filtered through a 70 µm mesh, and processed by droplet-based single-cell RNA-seq using the Chromium Next GEM Single Cell 3' GEM, Library & Gel Bead Kit v3.1 (10x Genomics, #1000121). Libraries were sequenced on a NovaSeq (Illumina).

Immunostaining and microscopy

Immunocytochemistry of 2D iPSC-derived cardiomyocytes

iPSC-derived CMs (d30) were detached using 10x TrypLE Select (Thermo Fisher Scientific, #A1217702),seeded on micropatterned slides (4D Cell, #MP-S-01) coated with Matrigel (Corning, #356231) three days prior to relaxation with 2,3-butanedione monoxime (BDM, Merck, #B0753) for 30 minutes and stained for α-sarcomeric ACTININ (Abcam, #ab9465, dilution 1:200) using goat-anti mouse IgG H&L Alexa Fluor 555 (Abcam, #ab150114, dilution 1:500) as previously described.[40] Sarcomere length was measured of line scans in myofibrils.

iPSC-derived CMs were detached using 10x TrypLE Select (Thermo Fisher Scientific, #A1217702), replated on chamber slides, and incubated for three days before staining on day 30. For sarcomeric proteins α-sarcomeric ACTININ (Abcam, #ab9465, dilution 1:200) and TNNT2 (Abcam, #ab8295, dilution 1:100) cells were fixed with 4% paraformaldehyde (Roth, #0335.2) for 10 minutes, washed, and permeabilized with PBS/0.25% Triton-X-100 for 10 minutes. After blocking with PBS/0.1% Triton-X-100 containing 5% normal goat serum (Abcam, #ab7481) for 1h, cells were incubated with first antibodies diluted in PBS/0.1% Triton-X-100 containing 1.5% normal goat serum overnight (4°C). After washing, secondary antibodies (goat-anti mouse IgG H&L Fluor 555, Abcam, #ab150114 and goat-anti mouse IgG H&L Fluor 488, Abcam, #ab150113) were added for 1h in the dark.

For CONNEXIN 40 (Abcam, #ab38580, dilution 1:100) and CONNEXIN 43 (Millipore, #MAB3068, dilution 1:100) staining, cells were fixed in ice-cold acetone (Roth, #CP40.1) for 10 minutes at -20°C, washed, and permeabilized with PBS/0.25% Triton-X-100 for 10 minutes. After blocking with PBS/0.1% Triton-X-100 containing 10% normal goat serum for 1h, cells were incubated with first antibodies diluted in PBS/0.1% Triton-X-100 containing 1.5% normal goat serum overnight (4°C). After washing, secondary antibodies (goat-anti rabbit IgG H&L Fluor 488, Abcam, #ab150077 and goat-anti mouse IgG H&L Fluor 555, Abcam, #ab150114) were added for 1h in the dark.

For all stainings, cells were washed three times with 1x PBS and once with *aq. bidest*, after incubation with secondary antibodies. Slides were air-dried, mounted in Fluoroshield Mounting Medium with DAPI (Abcam, #ab104139) and sealed with cover slides. All incubation steps were carried out at RT, unless otherwise specified.

Immunohistochemistry of 3D cardiac organoids

Fixed organoids were further processed for paraffin embedding and sectioning at the UKE pathology facility. Serial paraffin sections were acquired for histology staining of α-actinin (Sigma-Aldrich, #A7811), MLC2A (Synaptic Systems, #311011) and MLC2V (Synaptic Systems, #310111). Antigen retrieval was performed using Proteinase K for α-actinin, whereas citrate buffer was used for MLC2A and MLC2V. Primary antibodies were applied at the following dilutions: 1:600 for α-actinin, 1:20 for MLC2A, and 1:200 for MLC2V. Primary antibody binding was visualized with the multimer-technology based UltraView Universal DAB Detection kit (Ventana® BenchMark® XT; Roche, #460–500). Microscopic images were taken on an Axioskop 2 microscope (Zeiss).

Bright-field imaging and video acquisition

Photos and movies of 2D cultures were taken on a Nikon microscope (Nikon Corporation, Model Eclipse Ts2) using the TCapture software (Tucsen Photonics Co.Ltd.) version 5.1.1.

Microscopic images of the hHO were taken on the EVOS™ M5000 imaging system using the embedded software. Organoid culture progress and beating behavior were documented using the EVOS™ M5000 imaging system.

Evaluation of immunocytochemistry was performed using a fluorescence microscope (Axiovert 200M, Zeiss).

Measurement of ATP generation, glucose uptake and total cholesterol

ATP measurement

CellTiter-Glo® 2.0 assay (Promega, #G9241) was used to determine the number of viable cells in culture by quantifying the present ATP, indicating metabolically active cells according to the manufacturer´s instructions. Beating CPCs/early CMs (d08, d10, and d14) were detached using 10x TrypLE Select (Thermo Fisher Scientific, #A12177-02). A total of 20,000 cells were resuspended in 100 µL mTeSR™ Plus (StemCell Technologies, #100–0276) in a solid white flat-bottom polystyrene TC-treated microplate (Nunc™ MicroWell™ 96 Wells, Thermo Fisher Scientific, #136101). Standard curves were measured on each plate using ATP (Sigma, #A7699). The protocol was performed according to the manufacturer´s instructions. Luminescence was measured on an Infinity M200 PPO plate reader (Tecan) after 2 minutes of mixing on an orbital plate shaker (Heidolph, Polymax 1040) at 40 rpm to induce cell lysis, followed by

10 minutes of incubation at RT to stabilize the luminescent signal, with an integration time of 0.5 seconds per well.

Glucose-uptake assay

Glucose uptake in beating CPCs/early CMs (d08, d10, and d14) was measured using the Glucose Uptake-Glo™ Assay (Promega, #J1342), which detects 2-deoxyglucose-6-phosphate (2DG), following the manufacturer's protocol. Cells were detached using 10x TrypLE Select (Thermo Fisher Scientific). A total of 20,000 cells were resuspended in 25 µL mTeSR™ Plus (StemCell Technologies) and incubated for 15 minutes with 10 nM 2DG. Glucose Uptake-Glo™ Assay was performed as recommended by the manufacturer on a solid white flat-bottom polystyrene TC-treated microplate (Nunc™ MicroWell™ 96 Wells). Incubation with 10 nM 2DG was performed for 15 minutes. Luminescence signal was recorded on an Infinity M200 PPO plate reader (Tecan) with an integration time of 0.5 seconds per well after mixture for 60 seconds at 40 rpm on an orbital plate shaker (Heidolph) and incubation for 30 minutes at RT.

Cholesterol measurement

Cholesterol was measured using the Cholesterol/Cholesterol Ester-Glo™ Assay (Promega, #J3191) according to the manufacturer’s protocol. Beating CPCs/early CMs (d08, d10, and d14) were detached using 10x TrypLE Select (Thermo Fisher Scientific). 10,000 cells were resuspended in 25 µL mTeSR™ Plus (StemCell Technologies) on a solid white flat-bottom polystyrene TC-treated microplate (Nunc™ MicroWell™ 96 Wells). Luminescence signal was recorded on an Infinity M200 PPO plate reader (Tecan) with an integration time of 0.5 seconds per well after 60 seconds at 40 rpm on an orbital plate shaker (Heidolph) and 1 hour incubation at RT.

Appropriate controls for the CellTiter-Glo® 2.0 Assay, Cholesterol/Cholesterol Ester-Glo™ Assay, and Glucose Uptake-Glo™ Assay were included, according to the manufacturer´s recommendations.

Quantification and statistical analysis

Statistics

Statistical analyses were performed using R (version 4.2.0) or GraphPad Prism (version 10). R code was written by the authors and reviewed with assistance from ChatGPT (OpenAI). All code and resulting outputs were verified by the authors.

Unless stated otherwise, data are presented as mean ± standard deviation. Sstatistical tests and multiple-testing corrections are reported in the corresponding figure legends, exact P values are shown in the figures. Statistical tests were two-sided, and P values < 0.05 were considered statistically significant. For high-dimensional analyses, P values were adjusted using the Benjamini-Hochberg

correction. Exact sample sizes and the numbers of biological and technical replicates are reported in the corresponding figure legends.

Data availability

The genetic patient data reported in this study will be deposited in a public repository upon publication. Statistical analyses derived from these data are provided in the Supplementary Information. Additional data reported in this paper will be shared by the lead contact upon request.

Declarations

Conflict of interests

Dr. Krane is a physician proctor and a member of the medical advisory board for JOMDD and has received speakers' honoraria from EDWARDS, AtriCure, and Medtronic. The other authors report no conflicts.

Author contributions

Conceptualization, M.D., B.H.N., H.L., E.D., M.R., S.A.D., A.H., D.T., L.M.H., and M.K.; methodology, M.D., B.H.N., H.L., E.D., M.R., S.A.D., D.T., L.M.H., and M.K.; Investigation, M.D., B.H.N., H.L., I.G., S.R., D.B., F.W., S.S., E.D., M.R., and S.A.D.; writing – original draft, M.D. and B.H.N.; writing – review & editing, H.L., S.R., S.S., M.R., S.A.D., A.H., R.L., J.H., J.C., D.T., L.M.H., and M.K.; funding acquisition, A.H., L.M.H., and M.K.; resources, G.G., R.L., J.H., J.C., L.M.H., and M.K.; supervision, R.L., L.M.H., and M.K.

Acknowledgments

The authors are grateful for the participation of the HOS patient and the family members. The authors are thankful for the participation of the healthy proband. The authors thank Ivan Malcic, Department of Pediatrics, Division for Cardiology and Intensive Care Unit, University Hospital Zagreb, Zagreb, Croatia for support. The authors thank Xaver Reiminger for technical assistance in cell culture and performance of metabolic assays. The autors thank the KaBi-DHM (Cardiovascular Biobank of the TUM University Hospital German Heart Center, Technical University Munich).

This work was supported by grants from the German Research Foundation (KR3770/11 – 1 to Dr Krane, and HO5441/1–1 to Dr Holdt), German Center for Cardiovascular Research (DZHK-B 19-018SE to Dr Krane and Dr Hansen).

Dr. Dreßen is supported by Förderverein Deutschen Herzzentrum.

Code Availability

No custom code was developed for this study. All analyses were performed using standard functions in R and the specified R packages.

Gene expression analysis *in vitro* differentiation for the 2D and 3D model

Raw RNA-seq reads were adapter- and quality-trimmed using Cutadapt (version 3.7). Reads shorter than 20 nucleotides were discarded. Read quality was assessed using FastQC (version 0.11.9).

Trimmed paired-end reads were aligned to the human reference genome (GRCh38.p13) using HISAT2 (version 2.2.1) with downstream transcriptome assembly enabled (GENCODE release 42, GRCh38).

Transcript- and gene-level quantification was performed using StringTie (version 2.1.4) based on GENCODE release 41 annotations. Read counts were imported into R using tximport (version 1.24.0).

Differential gene expression analysis was performed using DESeq2 (version 1.26.0). For the 2D differentiation model (iPSC, d06, d08, d10, and d14), temporal expression dynamics were analyzed using a genotype × time interaction design. Genes with significant interaction effects were identified by likelihood ratio testing (LRT) and hierarchical clustering of variance-stabilized expression values. For the 3D differentiation model (d08, d10, and d15), stage-specific differential expression between genotypes was assessed using Wald tests with pairwise contrasts.

Gene expression estimates (FPKM) were also obtained using ballgown (version 2.28.0). Differentially expressed gene overlap was visualized with VennDiagram (version 1.7.3). Heatmaps of selected marker genes were generated from variance-stabilized expression values using hierarchical clustering and visualized with pheatmap (version 1.0.12). Expression values were row-centered before clustering.

Allele-specific expression analysis of 2D differentiation RNA-seq data

For allele-specific expression (ASE) analysis, RNA-seq reads were re-aligned with STAR-WASP to minimize reference mapping bias. ASE was quantified for rs1565941579 across all differentiation stages. The variant was annotated according to dbSNP build 154, and allele-specific read counts were obtained using GATK ASEReadCounter from WASP filtered reads.

Single-cell RNA-seq

Single-cell RNA sequencing (scRNA-seq) data from four human iPSC-derived CPC/CM samples collected on d08 of 2D differentiation, two samples each of 1460 and 1460c, were processed using Seurat (version 5.1.0). Filtered gene-barcode matrices generated with Cellranger (version 6.0.1) were imported using the Read10X-function. Quality control metrics, including detected genes, total UMI counts, and mitochondrial transcripts, were calculated per cell. Low-quality cells and outliers were removed using sample-specific thresholds based on visual inspection.

Datasets were independently log-normalized and highly variable genes were identified using Seurat's standard workflow. Cell barcodes were uniquely renamed to retain sample identity. Batch correction and data integration were performed using the Fast mutual nearest neighbors (FastMNN) algorithm. Dimensionality reduction was performed using Uniform Manifold Approximation and Projection (UMAP) on the MNN-corrected dimensions. Graph-based nearest-neighbor detection and unsupervised clustering were performed using the MNN space, with cluster resolution 0.8. Conserved markers across the two genotypes were identified using FindConservedMarkers, and cluster-specific differentially expressed genes were detected using FindAllMarkers (positive markers only; minimum detection fraction 25%; log fold-change threshold 0.25).

Cluster identities were visualized by UMAP and annotated using canonical markers.

Enrichment analyses

GSEA and over-representation analyses were performed using clusterProfiler (version 4.4.4) with MSigDB gene sets (release v2023.2).

For GSEA, genes were pre-ranked by log2 fold change and analyzed using the fgsea algorithm with 10,000 permutations and a P value cutoff of 0.2.

Over-representation analysis was performed using enricher, with detected genes as background. AnnotationDbi (version 1.58) and org.Hs.eg.db (version 3.15.0) were used for gene annotation.

ChIP–seq Peak Processing and Annotation

TBX5 ChIP–seq peak data[18] (GEO accession GSM2280011) were aligned to hg19 and provided in ENCODE narrowPeak format. Peak import and annotation were performed in R using *ChIPseeker* (version 1.32.1), based on GENCODE hg19 transcript annotations (GENCODE release 34, GRCh37). Promoter regions were defined as − 1,000 to + 500 bp relative to the transcription start site (TSS). Genes with promoter-associated TBX5 binding were extracted for downstream analyses.

Leading-Edge Analysis and Integration with TBX5 ChIP–seq Data

Stage-resolved leading-edge analyses were performed for selected GO biological process (GO-BP) terms from MSigDB (release v2023.2) using the R-package clusterProfiler (version 4.4.4). For each stage, genes were pre-ranked using DESeq2 interaction-term results comparing 1460 with 1460c and used for GSEA.

Leading-edge gene lists were generated for selected cardiac developmental and metabolic GO-BP terms. To identify TBX5-associated genes, leading-edge genes were intersected with promoter-associated TBX5 target genes.

For visualization, overlapping genes were prioritized based on their occurrence across differentiation stages and strength of the contributing enrichment signal. Heatmaps show the maximum absolute

normalized enrichment score (max |NES|) at the respective day.

Enrichment of leading-edge genes among promoter-associated TBX5 target genes was assessed by two-sided Fisher's exact test using all annotated genes as background. Odds ratios and 95% confidence intervals were calculated.

References

1. Brade, T., Pane, L. S., Moretti, A., Chien, K. R. & Laugwitz, K. L. Embryonic Heart Progenitors and Cardiogenesis. *Csh Perspect Med* 3, doi:ARTN a01384710.1101/cshperspect.a013847 (2013).
2. Dolk, H., Loane, M., Garne, E. & European Surveillance of Congenital Anomalies Working, G. Congenital heart defects in Europe: prevalence and perinatal mortality, 2000 to 2005. *Circulation* 123, 841–849, doi:10.1161/CIRCULATIONAHA.110.958405 (2011).
3. van der Linde, D. *et al.* Birth prevalence of congenital heart disease worldwide: a systematic review and meta-analysis. *J Am Coll Cardiol* 58, 2241–2247, doi:10.1016/j.jacc.2011.08.025 (2011).
4. Zaidi, S. & Brueckner, M. Genetics and Genomics of Congenital Heart Disease. *Circ Res* 120, 923–940, doi:10.1161/CIRCRESAHA.116.309140 (2017).
5. Basson, C. T. *et al.* Mutations in human TBX5 [corrected] cause limb and cardiac malformation in Holt-Oram syndrome. *Nat Genet* 15, 30–35, doi:10.1038/ng0197-30 (1997).
6. Weismann, C. G. & Gelb, B. D. The genetics of congenital heart disease: a review of recent developments. *Curr Opin Cardiol* 22, 200–206, doi:10.1097/HCO.0b013e3280f629c7 (2007).
7. Zaidi, S. *et al.* De novo mutations in histone-modifying genes in congenital heart disease. *Nature* 498, 220–223, doi:10.1038/nature12141 (2013).
8. Wimalasundera, R. C. & Gardiner, H. M. Congenital heart disease and aneuploidy. *Prenat Diagn* 24, 1116–1122, doi:10.1002/pd.1068 (2004).
9. Soemedi, R. *et al.* Contribution of global rare copy-number variants to the risk of sporadic congenital heart disease. *Am J Hum Genet* 91, 489–501, doi:10.1016/j.ajhg.2012.08.003 (2012).
10. Glessner, J. T. *et al.* Increased frequency of de novo copy number variants in congenital heart disease by integrative analysis of single nucleotide polymorphism array and exome sequence data. *Circ Res* 115, 884–896, doi:10.1161/CIRCRESAHA.115.304458 (2014).
11. Lahm, H. *et al.* Congenital heart disease risk loci identified by genome-wide association study in European patients. *J Clin Invest* 131, doi:10.1172/JCI141837 (2021).
12. Miyamoto, M., Gangrade, H. & Tampakakis, E. Understanding Heart Field Progenitor Cells for Modeling Congenital Heart Diseases. *Curr Cardiol Rep* 23, 38, doi:10.1007/s11886-021-01468-5 (2021).
13. Barisic, I. *et al.* Holt Oram syndrome: a registry-based study in Europe. *Orphanet J Rare Dis* 9, 156, doi:10.1186/s13023-014-0156-y (2014).

14. Holt, M. & Oram, S. Familial heart disease with skeletal malformations. *Br Heart J* 22, 236–242, doi:10.1136/hrt.22.2.236 (1960).
15. Newbury-Ecob, R. A., Leanage, R., Raeburn, J. A. & Young, I. D. Holt-Oram syndrome: a clinical genetic study. *J Med Genet* 33, 300–307, doi:10.1136/jmg.33.4.300 (1996).
16. Basson, C. T. *et al.* The clinical and genetic spectrum of the Holt-Oram syndrome (heart-hand syndrome). *N Engl J Med* 330, 885–891, doi:10.1056/NEJM199403313301302 (1994).
17. Steimle, J. D. & Moskowitz, I. P. TBX5: A Key Regulator of Heart Development. *Curr Top Dev Biol* 122, 195–221, doi:10.1016/bs.ctdb.2016.08.008 (2017).
18. Ang, Y. S. *et al.* Disease Model of GATA4 Mutation Reveals Transcription Factor Cooperativity in Human Cardiogenesis. *Cell* 167, 1734–1749 e1722, doi:10.1016/j.cell.2016.11.033 (2016).
19. Bruneau, B. G. *et al.* A murine model of Holt-Oram syndrome defines roles of the T-box transcription factor Tbx5 in cardiogenesis and disease. *Cell* 106, 709–721 (2001).
20. Papaioannou, V. E. & Silver, L. M. The T-box gene family. *Bioessays* 20, 9–19, doi:10.1002/(SICI)1521-1878(199801)20:1<9::AID-BIES4>3.0.CO;2-Q (1998).
21. Showell, C., Binder, O. & Conlon, F. L. T-box genes in early embryogenesis. *Dev Dyn* 229, 201–218, doi:10.1002/dvdy.10480 (2004).
22. Tsai, T. C. *et al.* The paracrine effect of exogenous growth hormone alleviates dysmorphogenesis caused by tbx5 deficiency in zebrafish (Danio rerio) embryos. *J Biomed Sci* 19, 63, doi:10.1186/1423-0127-19-63 (2012).
23. Ghosh, T. K. *et al.* Physical interaction between TBX5 and MEF2C is required for early heart development. *Mol Cell Biol* 29, 2205–2218, doi:10.1128/MCB.01923-08 (2009).
24. Lu, J. H. *et al.* Cascade effect of cardiac myogenesis gene expression during cardiac looping in tbx5 knockdown zebrafish embryos. *J Biomed Sci* 15, 779–787, doi:10.1007/s11373-008-9268-5 (2008).
25. Ahn, D. G., Kourakis, M. J., Rohde, L. A., Silver, L. M. & Ho, R. K. T-box gene tbx5 is essential for formation of the pectoral limb bud. *Nature* 417, 754–758, doi:10.1038/nature00814 (2002).
26. Garrity, D. M., Childs, S. & Fishman, M. C. The heartstrings mutation in zebrafish causes heart/fin Tbx5 deficiency syndrome. *Development* 129, 4635–4645 (2002).
27. Begemann, G. & Ingham, P. W. Developmental regulation of Tbx5 in zebrafish embryogenesis. *Mech Dev* 90, 299–304 (2000).
28. Bruneau, B. G. *et al.* Chamber-specific cardiac expression of Tbx5 and heart defects in Holt-Oram syndrome. *Dev Biol* 211, 100–108, doi:10.1006/dbio.1999.9298 (1999).
29. Chapman, D. L. *et al.* Expression of the T-box family genes, Tbx1-Tbx5, during early mouse development. *Dev Dyn* 206, 379–390, doi:10.1002/(SICI)1097-0177(199608)206:4<379::AID-AJA4>3.0.CO;2-F (1996).
30. McDermott, D. A. *et al.* TBX5 genetic testing validates strict clinical criteria for Holt-Oram syndrome. *Pediatr Res* 58, 981–986, doi:10.1203/01.Pdr.0000182593.95441.64 (2005).

31. Lichiardopol, C., Militaru, C., Popescu, B., Hila, G. & Mixich, F. Holt-Oram syndrome. *Rom J Morphol Embryol* 48, 67–70 (2007).
32. Malandraki-Miller, S., Lopez, C. A., Al-Siddiqi, H. & Carr, C. A. Changing Metabolism in Differentiating Cardiac Progenitor Cells-Can Stem Cells Become Metabolically Flexible Cardiomyocytes? *Front Cardiovasc Med* 5, 119, doi:10.3389/fcvm.2018.00119 (2018).
33. Lopaschuk, G. D. & Jaswal, J. S. Energy metabolic phenotype of the cardiomyocyte during development, differentiation, and postnatal maturation. *J Cardiovasc Pharmacol* 56, 130–140, doi:10.1097/FJC.0b013e3181e74a14 (2010).
34. Schenkel, L. C. & Bakovic, M. Formation and regulation of mitochondrial membranes. *Int J Cell Biol* 2014, 709828, doi:10.1155/2014/709828 (2014).
35. Martin, L. A., Kennedy, B. E. & Karten, B. Mitochondrial cholesterol: mechanisms of import and effects on mitochondrial function. *J Bioenerg Biomembr* 48, 137–151, doi:10.1007/s10863-014-9592-6 (2016).
36. Laudette, M. *et al.* PCSK9 Regulates Cardiac Mitochondrial Cholesterol by Promoting TSPO Degradation. *Circ Res* 136, 924–942, doi:10.1161/CIRCRESAHA.124.325629 (2025).
37. Dressen, M. *et al.* A novel de novo TBX5 mutation in a patient with Holt-Oram syndrome leading to a dramatically reduced biological function. *Mol Genet Genomic Med* 4, 557–567, doi:10.1002/mgg3.234 (2016).
38. Carvajal-Vergara, X. *et al.* Patient-specific induced pluripotent stem-cell-derived models of LEOPARD syndrome. *Nature* 465, 808–812, doi:10.1038/nature09005 (2010).
39. Ge, X. *et al.* Modeling supravalvular aortic stenosis syndrome with human induced pluripotent stem cells. *Circulation* 126, 1695–1704, doi:10.1161/CIRCULATIONAHA.112.116996 (2012).
40. Krane, M. *et al.* Sequential Defects in Cardiac Lineage Commitment and Maturation Cause Hypoplastic Left Heart Syndrome. *Circulation* 144, 1409–1428, doi:10.1161/CIRCULATIONAHA.121.056198 (2021).
41. Dressen, M. *et al.* Establishment of a patient-specific induced pluripotent stem cell line DHMi004-A from a male Holt-Oram syndrome patient with verified TBX5 mutation. *Stem Cell Res* 58, 102617, doi:10.1016/j.scr.2021.102617 (2022).
42. Lahm, H. *et al.* Correction of a deleterious TBX5 mutation in an induced pluripotent stem cell line (DHMi004-A-1) using a completely plasmid-free CRISPR/Cas 9 approach. *Stem Cell Res* 70, 103126, doi:10.1016/j.scr.2023.103126 (2023).
43. Dressen, M. *et al.* Establishment of an induced pluripotent stem cell line DHMi005-A from a healthy male proband. *Stem Cell Res* 59, 102662, doi:10.1016/j.scr.2022.102662 (2022).
44. Lahm, H. *et al.* Generation of a CRISPR/Cas edited human induced pluripotent stem cell line DHMi005-A-1 carrying a patient-specific disease-causing point mutation in the TBX5 gene. *Stem Cell Res* 60, 102691, doi:10.1016/j.scr.2022.102691 (2022).
45. Burridge, P. W., Holmstrom, A. & Wu, J. C. Chemically Defined Culture and Cardiomyocyte Differentiation of Human Pluripotent Stem Cells. *Curr Protoc Hum Genet* 87, 21 23 21 – 15,

doi:10.1002/0471142905.hg2103s87 (2015).

46. Luna-Zurita, L. *et al.* Complex Interdependence Regulates Heterotypic Transcription Factor Distribution and Coordinates Cardiogenesis. *Cell* 164, 999–1014, doi:10.1016/j.cell.2016.01.004 (2016).
47. Lewis-Israeli, Y. R. *et al.* Self-assembling human heart organoids for the modeling of cardiac development and congenital heart disease. *Nat Commun* 12, 5142, doi:10.1038/s41467-021-25329-5 (2021).
48. Cui, Y. *et al.* Single-Cell Transcriptome Analysis Maps the Developmental Track of the Human Heart. *Cell Rep* 26, 1934–1950 e1935, doi:10.1016/j.celrep.2019.01.079 (2019).
49. Moller Nielsen, A. K., Dehn, A. M., Hjortdal, V. & Larsen, L. A. TBX5 variants and cardiac phenotype: A systematic review of the literature and a novel variant. *Eur J Med Genet* 68, 104920, doi:10.1016/j.ejmg.2024.104920 (2024).
50. Hiroi, Y. *et al.* Tbx5 associates with Nkx2-5 and synergistically promotes cardiomyocyte differentiation. *Nat Genet* 28, 276–280, doi:10.1038/90123 (2001).
51. Karakikes, I. *et al.* A Comprehensive TALEN-Based Knockout Library for Generating Human-Induced Pluripotent Stem Cell-Based Models for Cardiovascular Diseases. *Circ Res* 120, 1561–1571, doi:10.1161/CIRCRESAHA.116.309948 (2017).
52. Burridge, P. W. *et al.* Chemically defined generation of human cardiomyocytes. *Nat Methods* 11, 855–860, doi:10.1038/nmeth.2999 (2014).
53. Garg, V. *et al.* GATA4 mutations cause human congenital heart defects and reveal an interaction with TBX5. *Nature* 424, 443–447, doi:10.1038/nature01827 (2003).
54. Durocher, D., Charron, F., Warren, R., Schwartz, R. J. & Nemer, M. The cardiac transcription factors Nkx2-5 and GATA-4 are mutual cofactors. *EMBO J* 16, 5687–5696, doi:10.1093/emboj/16.18.5687 (1997).
55. Cai, C. L. *et al.* T-box genes coordinate regional rates of proliferation and regional specification during cardiogenesis. *Development* 132, 2475–2487, doi:10.1242/dev.01832 (2005).
56. Singh, M. K. *et al.* Tbx20 is essential for cardiac chamber differentiation and repression of Tbx2. *Development* 132, 2697–2707, doi:10.1242/dev.01854 (2005).
57. Stennard, F. A. *et al.* Murine T-box transcription factor Tbx20 acts as a repressor during heart development, and is essential for adult heart integrity, function and adaptation. *Development* 132, 2451–2462, doi:10.1242/dev.01799 (2005).
58. Stennard, F. A. & Harvey, R. P. T-box transcription factors and their roles in regulatory hierarchies in the developing heart. *Development* 132, 4897–4910, doi:10.1242/dev.02099 (2005).
59. Stennard, F. A. *et al.* Cardiac T-box factor Tbx20 directly interacts with Nkx2-5, GATA4, and GATA5 in regulation of gene expression in the developing heart. *Dev Biol* 262, 206–224, doi:10.1016/s0012-1606(03)00385-3 (2003).

60. Arduini, A. *et al.* Transcriptional profile of the rat cardiovascular system at single-cell resolution. *Cell Rep* 44, 115091, doi:10.1016/j.celrep.2024.115091 (2025).
61. Abdelwahid, E., Pelliniemi, L. J. & Jokinen, E. Cell death and differentiation in the development of the endocardial cushion of the embryonic heart. *Microsc Res Tech* 58, 395–403, doi:10.1002/jemt.10159 (2002).
62. Lin, C. J., Lin, C. Y., Chen, C. H., Zhou, B. & Chang, C. P. Partitioning the heart: mechanisms of cardiac septation and valve development. *Development* 139, 3277–3299, doi:10.1242/dev.063495 (2012).
63. Wu, B. *et al.* Developmental Mechanisms of Aortic Valve Malformation and Disease. *Annu Rev Physiol* 79, 21–41, doi:10.1146/annurev-physiol-022516-034001 (2017).
64. O'Donnell, A. & Yutzey, K. E. Mechanisms of heart valve development and disease. *Development* 147, doi:10.1242/dev.183020 (2020).
65. Shu, S. *et al.* Cellular Landscapes of Nondiseased Human Cardiac Valves From End-Stage Heart Failure-Explanted Heart. *Arterioscler Thromb Vasc Biol* 42, 1429–1446, doi:10.1161/ATVBAHA.122.318314 (2022).
66. Liu, Z. *et al.* APOE-NOTCH axis governs elastogenesis during human cardiac valve remodeling. *Nat Cardiovasc Res* 3, 933–950, doi:10.1038/s44161-024-00510-3 (2024).
67. Zhao, R. *et al.* Single-Cell Transcriptomics Identified Fibrosis-Activated Valve Interstitial Cells Involved in Functional Tricuspid Regurgitation. *JACC Asia* 5, 478–495, doi:10.1016/j.jacasi.2025.01.013 (2025).
68. Blanchet, E. *et al.* E2F transcription factor-1 regulates oxidative metabolism. *Nat Cell Biol* 13, 1146–1152, doi:10.1038/ncb2309 (2011).
69. Steimle, J. D. *et al.* Single-nuclei transcriptomics reveals TBX5-dependent targets in a patient with Holt-Oram syndrome. *J Clin Invest* 135, doi:10.1172/JCI180670 (2024).
70. Crilley, J. G. *et al.* Hypertrophic cardiomyopathy due to sarcomeric gene mutations is characterized by impaired energy metabolism irrespective of the degree of hypertrophy. *J Am Coll Cardiol* 41, 1776–1782, doi:10.1016/s0735-1097(02)03009-7 (2003).
71. Sambandam, N., Lopaschuk, G. D., Brownsey, R. W. & Allard, M. F. Energy metabolism in the hypertrophied heart. *Heart Fail Rev* 7, 161–173, doi:10.1023/a:1015380609464 (2002).
72. Aoyama, R. *et al.* Evaluation of myocardial glucose metabolism in hypertrophic cardiomyopathy using 18F-fluorodeoxyglucose positron emission tomography. *PLoS One* 12, e0188479, doi:10.1371/journal.pone.0188479 (2017).
73. Jung, W. I. *et al.* 31P NMR spectroscopy detects metabolic abnormalities in asymptomatic patients with hypertrophic cardiomyopathy. *Circulation* 97, 2536–2542, doi:10.1161/01.cir.97.25.2536 (1998).
74. Reyat, J. S. *et al.* PITX2 deficiency leads to atrial mitochondrial dysfunction. *Cardiovasc Res* 120, 1907–1923, doi:10.1093/cvr/cvae169 (2024).

75. Sun, Q., Karwi, Q. G., Wong, N. & Lopaschuk, G. D. Advances in myocardial energy metabolism: metabolic remodelling in heart failure and beyond. *Cardiovasc Res* 120, 1996–2016, doi:10.1093/cvr/cvae231 (2024).
76. Wang, S. *et al.* PALMD regulates aortic valve calcification via altered glycolysis and NF-kappaB-mediated inflammation. *J Biol Chem* 298, 101887, doi:10.1016/j.jbc.2022.101887 (2022).
77. Aycinena, J. *et al. Plakophilin-2 Coordinates Energy Metabolism and Contractility in Cardiomyocytes, Revealing Its Roles beyond Desmosomes*. (2025).
78. Farhat, B. *et al.* Understanding the cell fate and behavior of progenitors at the origin of the mouse cardiac mitral valve. *Dev Cell* 59, 339–350 e334, doi:10.1016/j.devcel.2023.12.006 (2024).
79. Fahed, A. C., Gelb, B. D., Seidman, J. G. & Seidman, C. E. Genetics of congenital heart disease: the glass half empty. *Circ Res* 112, 707–720, doi:10.1161/CIRCRESAHA.112.300853 (2013).

Figures

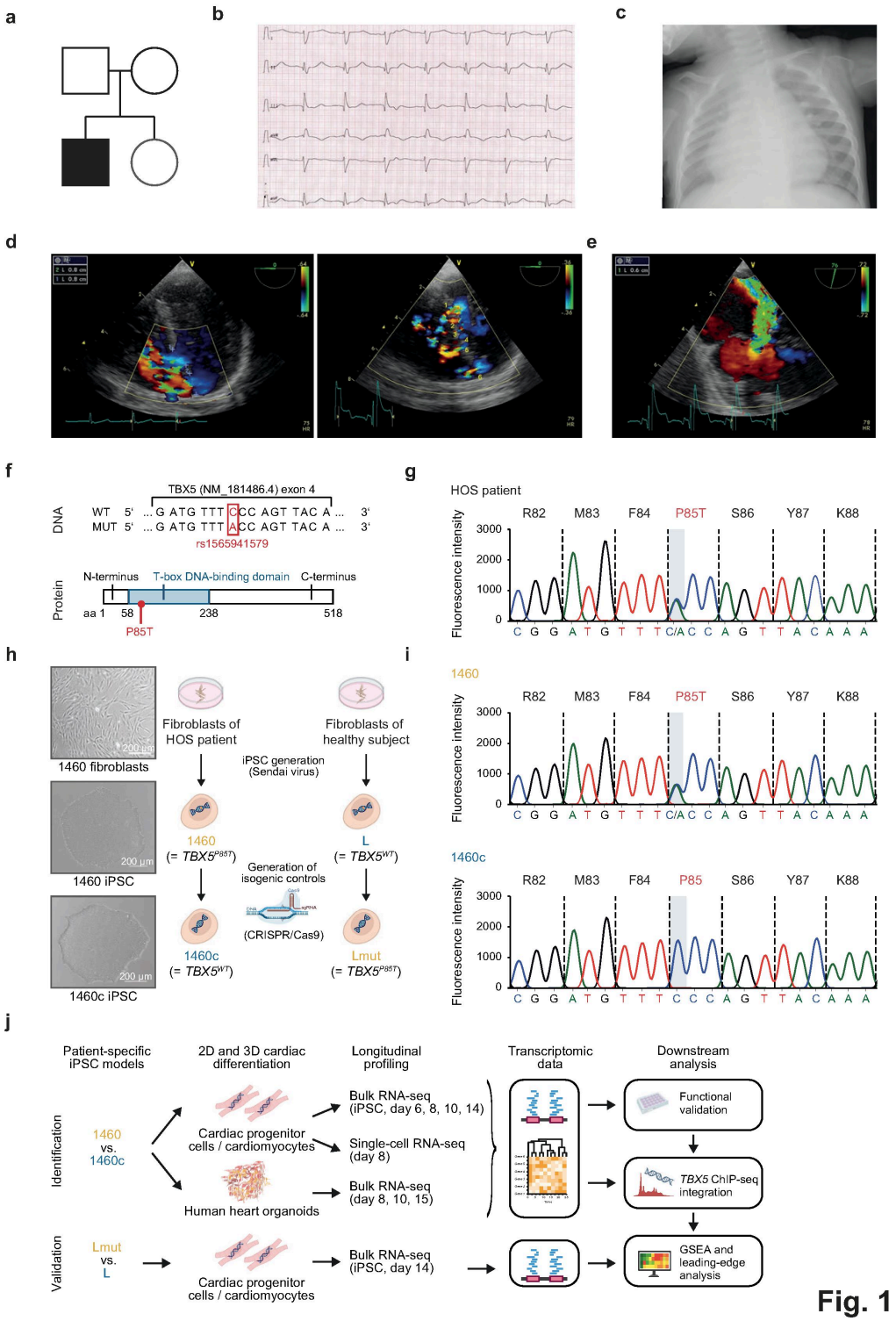


Fig. 1

Figure 1

Heterozygous *de novo TBX5* mutation leads to Holt-Oram Syndrome, manifesting in a severe clinical phenotype

a Pedigree of the affected Holt-Oram Syndrome (HOS) patient showing the healthy parents and the female sibling with atrial septal defect II. Circles represent females, and squares represent males. Open

symbols indicate no diagnosis of HOS. Filled symbols indicate HOS. Grey symbols indicates atrial septal defect II.

b Resting electrocardiogram of the patient showing no signs of arrhytmia.

c Chest X-ray showing an enlarged heart in the patient.

d Transesophageal echocardiography (TEE) with mid esophageal views in 0° (four chamber view) showing multiple ventricular septal defects.

e TEE in mid esophageal short axis (76°) showing the dysplastic tricuspid valve.

f Location of the identified *TBX5*mutation (rs1565941579: C>A, NM_181486.4) in exon 4 within the affected gene locus (MUT) and corresponding protein TBX5 (NP_852259.1; UniProt: Q99593).

g Sanger sequencing of exon 4 (NM_181486.4) confirming the heterozygous nucleotide change leading to an amino acid change at position 85 from proline to threonine (NP_852259.1:p.Pro85Thr).

h Generation of the patient-specific 1460/1460c pair and the independent Lmut/L validation pair. Left, representative phase-contrast images of the patient´s fibroblasts before reprogramming, and colonies of iPSC line 1460 and the CRISPR/Cas9-corrected isogenic iPSC line 1460c. Scale bars: 200 µm. Right, schematic illustration of reprogramming from adipose fibroblasts and correction of the *TBX5* mutation in the patient-specific iPSC line. For independent validation in a second genetic background, the *TBX5* Pro85Thr mutation was introduced into the healthy donor-derived iPSC line L to generate the isogenic mutant line Lmut.

i Sanger sequencing chromatograms validating the heterozygous mutation in the patient-specific iPSC line 1460 and the correction of the mutation in the iPSC line 1460c.

j Schematic overview of 2D and 3D cardiac differentiation, longitudinal transcriptomic profiling, and downstream analyses in the patient-specific 1460/1460c pair. The independent Lmut/L pair was used for validation in a second genetic background.

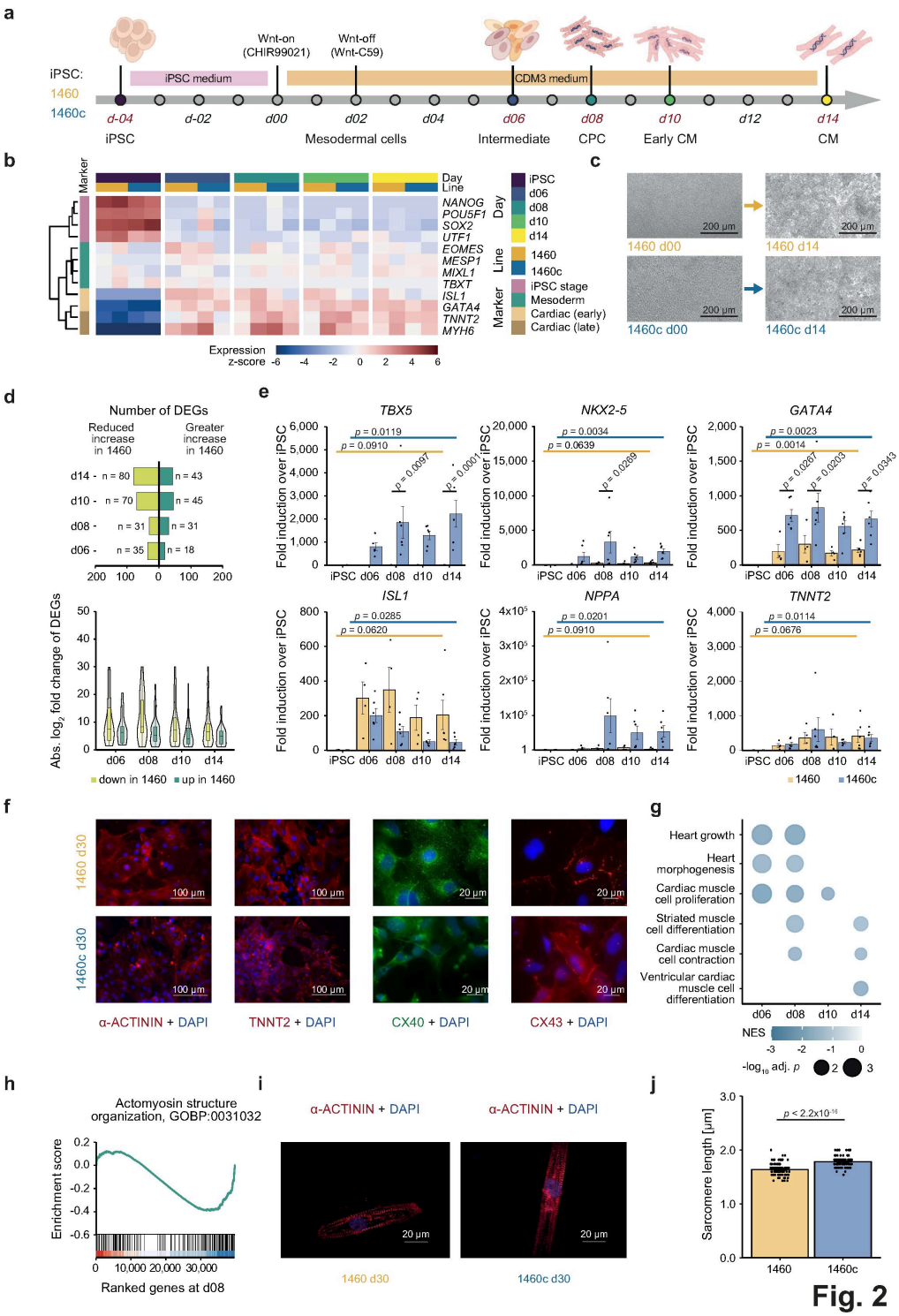


Fig. 2

Figure 2

In vitro analysis indicates dysregulation of core cardiac transcription factors in *TBX5*-mutated Cardiac Progenitor Cells and impaired Cardiomyocytes maturation

a Cardiac differentiation protocol based on Wnt-signaling modulation. Cell states from iPSC through mesodermal, intermediate and cardiac progenitor cell (CPC) stages to cardiomyocytes (CMs) are

indicated. RNA-seq time points are marked in color.

b Representative markers for the iPSC stage, mesoderm and early and late cardiac development stages. Expression levels are shown as normalized z-scores from two differentiations per line.

c Representative bright-field images of monolayers of seeded single cells (d00) and differentiated cardiomyocytes (d14). Scale bars: 200 µm.

d Stage-specific bulk RNA-seq profiling across cardiac differentiation revealed genotype-dependent differences in gene expression trajectories. Top, number of genes identified at d06, d08, d10 and d14, separated into genes with reduced or greater increase in 1460. Bottom, distribution of absolute log2 fold changes of these differentially expressed genes (adjusted $P < 0.05$ and |log2 fold change| > 1) across time points.

e Induction of the cardiac transcription factors *TBX5*, *NKX2-5*, *GATA4*, *ISL1, NPPA*, and *TNNT2* relative to iPSC. Fold gene expression was determined by qRT-PCR after normalization to *a-actin* (*ACTB*). Data were generated from independent differentiations (n = 3) with biological duplicates (1460) and triplicates (1460c). Data are mean±SEM. Data were analyzed by unpaired Student´s *t* test and ANOVA with multiple-testing correction. Exact *P* values are indicated in the figure.

f Representative immunostaining of cardiomyocytes (d30) for a-ACTININ (red), TNNT2 (red), CX40 (green), CX43 (red), and DAPI (blue). Scale bars: 100 µm for a-ACTININ and TNNT2, 20 µm for CX40 and CX43.

g Stage-resolved GSEA of selected cardiac-related GO biological process (GO-BP) terms across differentiation. Semantically reduced GO-BP terms related to cardiac development and function are shown for the comparison of lineage 1460 with 1460c. Point size indicates $-\log_{10}$ adjusted *P* value and colour indicates normalized enrichment score (NES). Benjamini-Hochberg corrected adjusted P values are shown.

h Running enrichment score plot for actomyosin structure organization (GOBP:0031032) at day 8 comparing lineage 1460 with 1460c.

i Representative immunostaining for a-ACTININ in day-30 cardiomyocytes derived from lines 1460 and 1460c, showing sarcomeric organization. Scale bars: 20 µm.

j Quantification of sarcomere length in day-30 cardiomyocytes stained for a-ACTININ after treatment with 2,3-butanedione monoxime (BDM). Sarcomere length was quantified from n = 186 measurements in 49 CMs in 1460 and n = 116 measurements in 42 CMs in 1460c. Data are mean±SEM. Data were analyzed using a two-sided Mann-Whitney rank-sum test. Exact *P* value is indicated in the figure.

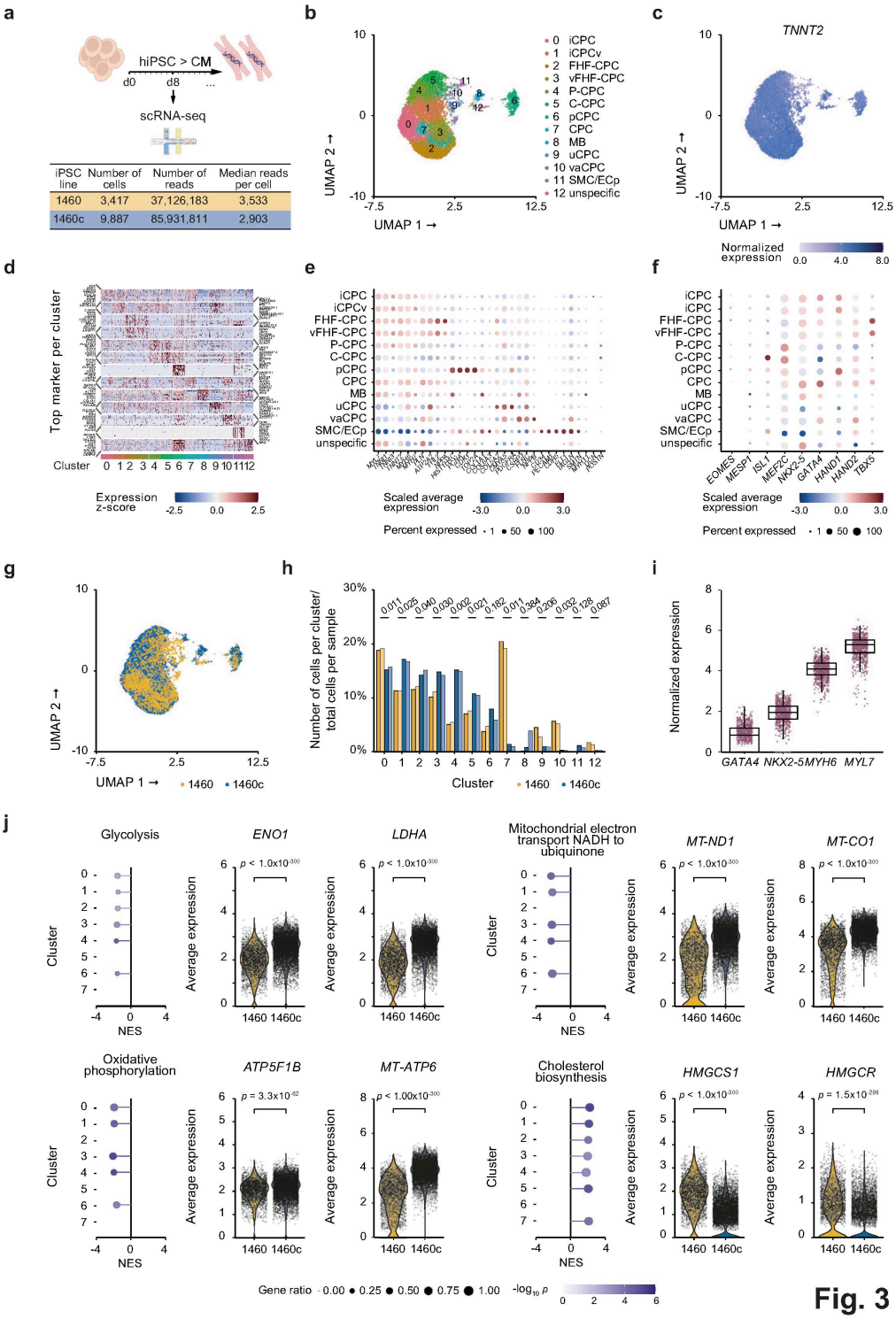


Fig. 3

Figure 3

Single-cell RNA sequencing of beating *TBX5*-mutated Cardiac Progenitor Cells uncovers disrupted energy metabolism and cholesterol homeostasis

a Schematic of single-cell RNA-seq analysis at day 8 of 2D cardiac differentiation, including the number of cells, reads, and median reads per cell for lines 1460 and 1460c.

b Dimensionally reduced map using uniform manifold approximation and projection (UMAP) for all cell populations captured at day 8. Each cluster in the reduced map represents a distinct cell-type identity. iCPC (0), immature CPC; iCPCv (1), immature ventricular CPC; FHF-CPC (2), committed FHF CPC; vFHF-CPC (3), committed ventricular FHF CPC; P-CPC (4), precursor CPC; C-CPC (5), common CPC; pCPC (6), proliferating CPC; CPC (7), CPC; MB (8), myoblasts; uCPC (9), unspecific CPC; vaCPC (10), vascular CPC; SMC/ECp (11), smooth muscle cell/endothelial cell progenitors; unspecific (12), unspecific cells. CPC, cardiac progenitor cell. FHF, first heart field.

c Dimensionally reduced map using the UMAP technique showing normalized expression of *TNNT2*.

d Heatmap showing scaled z-scores of average expression levels of the top differentially expressed genes for each cluster.

e, **f** Scaled average expression of cell-type-specific markers (**e**) and cell-lineage-specific transcription factors (**f**) across all cells in different cell types.

g Dimensionally reduced UMAP of all cell-type identities split by line.

h Percentage of cells per cluster relative to the total number of cells per sample, split by line (1460, 1460c) across assay (1460: n = 2, 1460c: n = 2). Exact *P*values are indicated in the figure.

i Normalized expression of *GATA4*, *NKX2-5*, *MYH6*, and *MYL7* in CPCs (cluster 7).

j Normalized enrichment score (NES) of dysregulated genes (1460 vs. 1460c, day 8) in clusters 0 to 7 associated with glycolysis, mitochondrial electron transport NADH to ubiquinone, oxidative phosphorylation, and cholesterol biosynthesis. NES, gene ratio and adjusted *P* value are given. For each pathway, average expression of two representative dysregulated genes (glycolysis: *ENO1* and *LDHA*; mitochondrial electron transport from NADH to ubiquinone: *MT-ND1* and *MT-CO1*; oxidative phosphorylation: *ATP5F1B* and *MT-ATP6*; cholesterol biosynthesis: *HMGCS1* and *HMGCR*) split by genotype for clusters 0-7 are shown. *P* values were calculated using the Wald test. Exact values are indicated in the figure, and $P < 0.05$ was considered statistically significant.

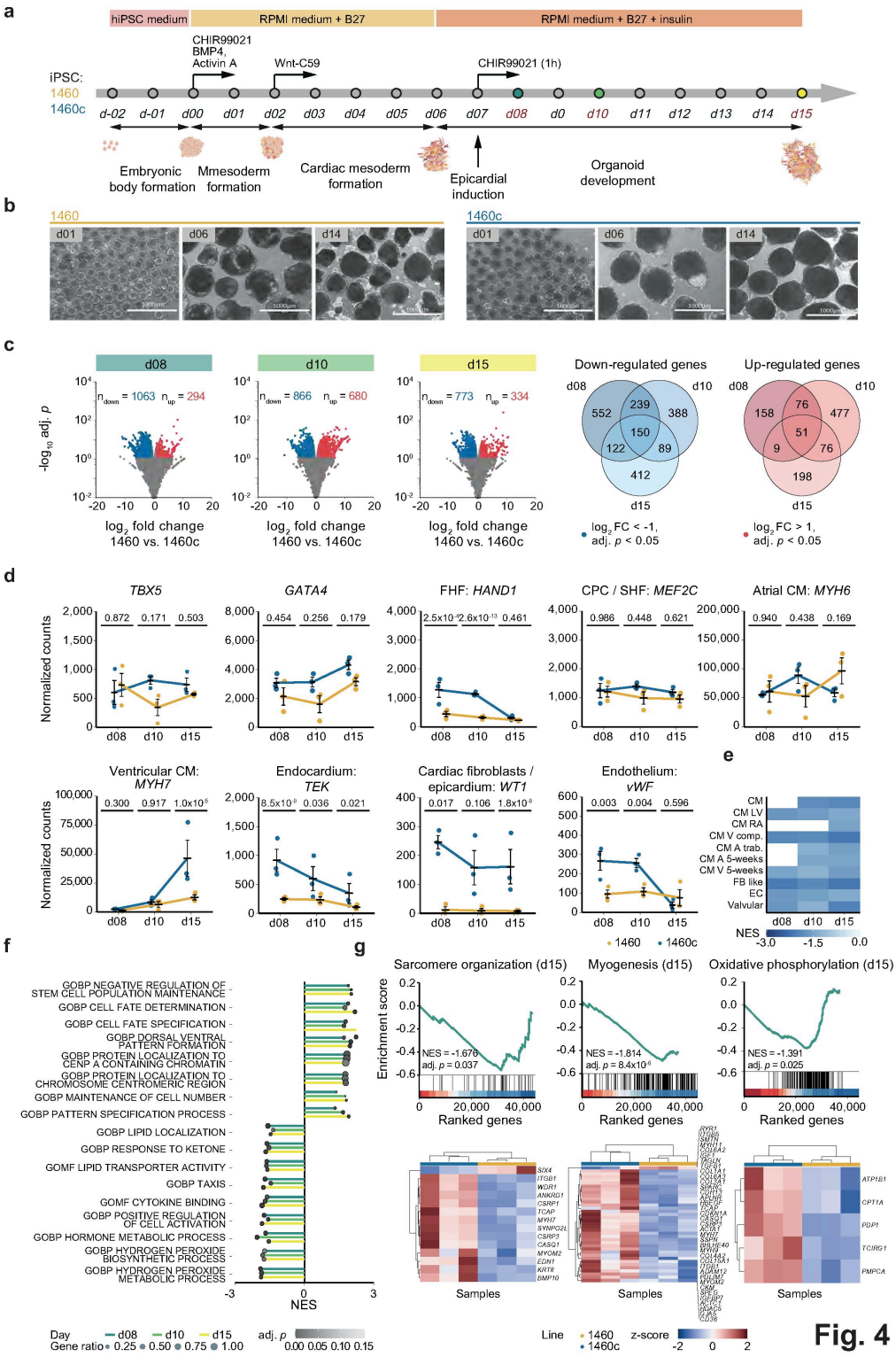


Fig. 4

Figure 4

Multicellular 3D-Model of *TBX5*-mutated Human Heart Organoids reveals disruptions in energy metabolism, cholesterol homeostasis, and cytoskeletal architecture

a Schematic of human heart organoid (hHO) differentiation using a three-step WNT-signaling protocol. RNA-seq time points are indicated at days 8, 10 and 15.

b Bright-field images showing the morphology of developing organoids at day 1, 6, and 14 for both iPSC lines. Scale bars: 1000 µm.

c Differential gene expression across hHO differentiation. Left, volcano plots for all stages highlight differentially expressed genes (DEGs) with $|\log_2$ fold change$| > 1$ and adjusted $P < 0.05$. Right, Venn diagrams show overlap for downregulated DEGs (blue) and upregulated DEGs (red) across all stages.

d Expression of lineage-associated marker genes. Normalized counts for *TBX5* and *GATA4* (heterotypic transcription factors), FHF (*HAND1*), CPC/SHF (*MEF2C*), atrial CM (*MYH6*), ventricular CM (*MYH7*), endocardium (*TEK*), cardiac fibroblasts/epicardium (*WT1*), and endothelium (*vWF*) are shown across all stages (n = 3 replicates per line). Data are presented as mean±SEM. *P* values were calculated by Wald test and corrected by the Benjamini–Hochberg method. Exact *P* values are indicated in the figure. FHF, first heart field; CPC, cardiac progenitor cells; SHF, second heart field; CM, cardiomyocytes.

e Cell-type-resolved GSEA based on fetal heart reference signatures. Normalized enrichment scores (NES) are shown for all stages using single-cell RNA sequencing signatures from normal fetal hearts between 4.5 and 25 weeks of gestation[48]. CM, cardiomyocytes; CM LV, left ventricular cardiomyocytes; CM RA, right atrial cardiomyocytes; CM V comp., compact ventricular cardiomyocytes; CM A trab., trabecular atrial cardiomyocytes; CM A 5-weeks, atrial cardiomyocytes at 5 weeks of gestation; CM V 5-weeks, ventricular cardiomyocytes at 5 weeks of gestation; FB-like, fibroblast-like cells; EC, endothelial cells; Valvular, valvular cells.

f Dot plot of selected cardiac and metabolic GO-BP terms across all differentiation stages. Colour indicates stage, dot size indicates gene ratio, and dot shading indicates adjusted P value. Adjusted P values were corrected by the Benjamini–Hochberg method.

g Selected pathways at day 15. Top, enrichment plots for sarcomere organization, myogenesis and oxidative phosphorylation at day 15 with NES and adjusted P values. Bottom, heatmaps show expression of contributing genes as normalized z-scores.

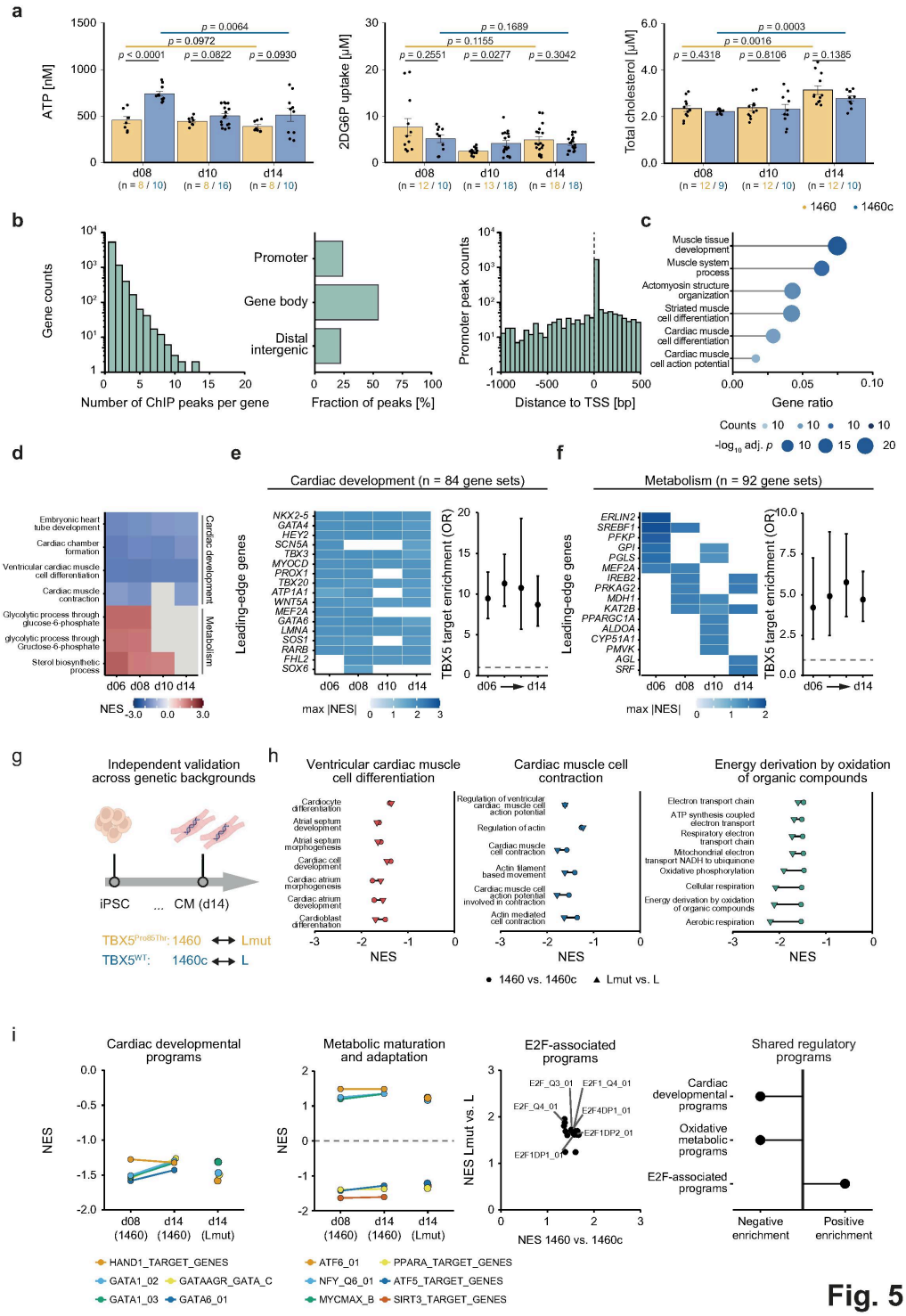


Fig. 5

Figure 5

Validation of metabolic disturbances and TBX5 binding to metabolic regulators in HOS-derived Cardiac Progenitor Cells and early Cardiomyocytes

a Metabolic assays during cardiac differentiation (2D model). ATP levels, glucose uptake, and total cholesterol were measured at days 8, 10, and 14. Data were generated from independent differentiations

with biological duplicates; the number of measurements is indicated in the plot. Data are mean±SEM. Outliers were identified by Grubbs test at a 10% significance level. *P* values were calculated using an unpaired two-tailed Student's t-test. Exact *P* values are indicated in the figure.

b Published TBX5 ChIP-seq dataset in iPSC-derived cardiomyocytes at day 32 from Ang et al[18]. Left, distribution of TBX5 ChIP peaks per gene. Middle left, genomic annotation of TBX5 peaks. Right, distribution of promoter-associated TBX5 peaks relative to the transcription start site (TSS).

c Functional annotation of promoter-associated TBX5 target genes. Enrichment of semantically reduced cardiac developmental and structural GO biological process (GO-BP) terms is shown with gene ratio, counts, and and adjusted *P* values. Adjusted *P* values were corrected using the Benjamini-Hochberg procedure.

d Stage-resolved GSEA of selected cardiac developmental and metabolic GO-BP terms across 2D differentiation. Normalized enrichment scores (NES) comparing lineage 1460 with 1460c are shown for days 6, 8, 10, and 14.

e, f TBX5 promoter target genes overlapping with leading-edge genes from (**e**) cardiac developmental (n = 84 GO-BP gene sets) and (**f**) metabolic (n = 92 GO-BP gene sets) programs identified by stage-resolved GSEA. Left, heatmaps show selected overlapping genes across stages. Colour indicates the maximum absolute normalized enrichment score (max |NES|) of the contributing gene set at the respective day. Right, enrichment of genes in TBX5 promoter targets was assessed by two-sided Fisher’s exact test using all annotated genes as background. Points indicate odds ratios (OR) and error bars 95% confidence intervals.

g Independent validation across genetic backgrounds. The TBX5Pro85Thr mutant line 1460 and its isogenic control 1460c were compared with the independent mutant-control pair Lmut and L. Both pairs were differentiated from iPSCs to cardiomyocytes with transcriptomic profiling at day 14.

h Validation of concordant GO-BP processes in the independent Lmut line at day 14. GO-BP gene sets were grouped into semantically related processes based on GO term. Selected GO-BP terms contributing to ventricular cardiac muscle cell differentiation, cardiac muscle cell contraction, and energy derivation by oxidation of organic compounds with the same direction of enrichment in 1460 vs. 1460c and Lmut vs. L are shown.

i Concordant regulatory gene sets across both genetic backgrounds. GSEA of MSigDB C3 transcription factor target (TFT) gene sets were used to assess cardiac developmental and metabolic maturation and adaptation programs at days 8 and 14 in 1460 and at day 14 in Lmut. E2F-associated programs are shown to exhibit concordant enrichment by NES comparison between 1460 and Lmut at day 14. Right, shared cardiac developmental, oxidative metabolic, and E2F-associated programs are summarized according to their direction of enrichment.

Supplementary Files

This is a list of supplementary files associated with this preprint. Click to download.

- VideoS5.1460ciPSCderivedCMsD14.avi
- SupplementaryFiguresS1S7.pdf
- VideoS3.1460iPSCderivedCMsD30.avi
- VideoS2.1460iPSCderivedCMsD14.avi
- VideoS8.1460hHOD15.mp4
- VideoS1.1460iPSCderivedCPCsD8.avi
- SupplementaryDataSets116.xlsx
- VideoS4.1460ciPSCderivedCPCsD8.avi
- VideoS6.1460ciPSCderivedCMsD30.avi
- VideoS10.1460chHOD15.mp4
- VideoS9.1460chHOD8.mp4
- VideoS7.1460hHOD8.mp4